Fabrication of Tungsten Oxide Thin Film on Stainless Steel by Sol-Gel Method.

By

Geoffrey Momanyi

Submitted in Partial Fulfillment of the Requirements

For The Degree of

Master of Science

in the

Chemistry

Program

YOUNGSTOWN STATE UNIVERSITY

May, 2023

Fabrication of Tungsten Oxide Thin Film on Stainless Steel by Sol-Gel Method.

Geoffrey Ogoso Momanyi

I hereby release this thesis to the public. I understand that this thesis will be made available from the Ohio LINK ETD Center and the Maag Library Circulation Desk for public access. I also authorize the University or other individuals to make copies of this thesis as needed for scholarly research.

Signature:

…….

Geoffrey Ogoso Momanyi, Student **Date**

Approvals:

…..……

Dr. Clovis A. Linkous, Thesis Advisor **Date**

…..……

Dr. Timothy R. Wagner, Committee Member **Date**

…..……

Dr. Christopher Arntsen, Committee Member **Date**

…..……

Dr. Salvatore A. Sanders, Dean of Graduate Studies **Date**

ABSTRACT

Metal oxide semiconductor materials such as tungsten oxide are promising candidates for use as photoanodes in solar water splitting. Tungsten oxide is an n-type semiconductor that was prepared on stainless steel 304 substrate and subsequently studied for water-splitting applications. This study investigated the effect of the annealing temperature and substrate cleaning reagents on the photoelectrochemical (PEC) properties of tungsten oxide thin films. The main method of synthesis employed was the sol-gel method. Tungsten oxide thin films were deposited from a precursor solution of peroxotungstic acid by doctor blading. The as-deposited amorphous WO_3 films were further subjected to heat treatment at various annealing temperatures (200 °C, 300 °C, 400 °C, and 500 °C) to transform the amorphous material into polycrystalline WO_3 nanostructures. Surface morphology, the crystallinity of the film, the thickness of the film, and photoelectrochemical properties were investigated using scanning electron microscopy, (SEM), X-ray diffractometry (XRD), stylus profilometry, cyclic voltammetry (CV) and linear sweep voltammetry (LSV). The optimal WO_3 film, at a thickness of 5 μm and annealed at 400 °C, achieved a photocurrent density of 98.0 $\mu A/cm^2$ at an applied voltage of 0.53 V vs Ag/AgCl. It is essential to treat the substrate with HNO_3 to passivate the surface of the stainless-steel substrate with the Cr_2O_3 layer.

ACKNOWLEDGEMENT

First, I would like to thank my research advisor, Dr. Clovis A. Linkous, for his sincere support and for allowing me to work with him. His patience, immense knowledge, and encouragement will not go unnoticed. He was always there for me, and he never gave up on me despite the frequent visits to his office. I also thank my committee members, Dr. Timothy R. Wagner, and Dr. Christopher Arntsen, for accepting to be on the committee and for their contributions to this research. I genuinely appreciate the Department of Chemical and Biological Sciences for allowing me to study at Youngstown State University. I would also like to thank Ray Hoff for his support with the instruments. My thanks to fellow students, Kim, Moses, Silas, and Onyinyechukwu for their support.

My faith in God helped me during difficult times, and through the grace of the Almighty, I navigated on through the past two academic years. Thank you, Lord, for standing with me always. I thank my family and friends for constantly encouraging me. My special thanks go to my dear wife, Ruth, who consistently motivated me to press on. She was the pillar of my strength and a source of hope. My kids Jasmine, Jamila, and Jayden, you were the primary reason for my hard work. Finally, my prayerful mother, Peninah, I know you always pray for my success, and I sincerely appreciate your efforts.

TABLE OF CONTENTS

LIST OF TABLES……ix

LIST OF FIGURES

CHAPTER 1. ENERGY

1.1 Introduction

Energy is a very crucial and fundamental resource in human life. The reason is that almost every household requires energy for its operation. Energy exists in the form of electrical, thermal, chemical, or mechanical. A fundamental dichotomy between the many energy resources is those which are renewable and those which are non-renewable.

Renewable resources can be replenished, and someone can no longer reuse non-renewable resources since they can be depleted. However, non-renewable resources are majorly fossil based, about 80% of the world's energy consumption. The significant non-renewable resources include coal, petroleum, and natural gas among others. Renewable resources can be replenished and hence can never be exhausted. They include solar energy, wind energy, biomass, ocean current, tidal, and geothermal among others.

Sources show that forms of fossil fuel energy are the most produced in the US. Figure 1 below shows a simple comparison of different forms of energy in 2020 in the US.

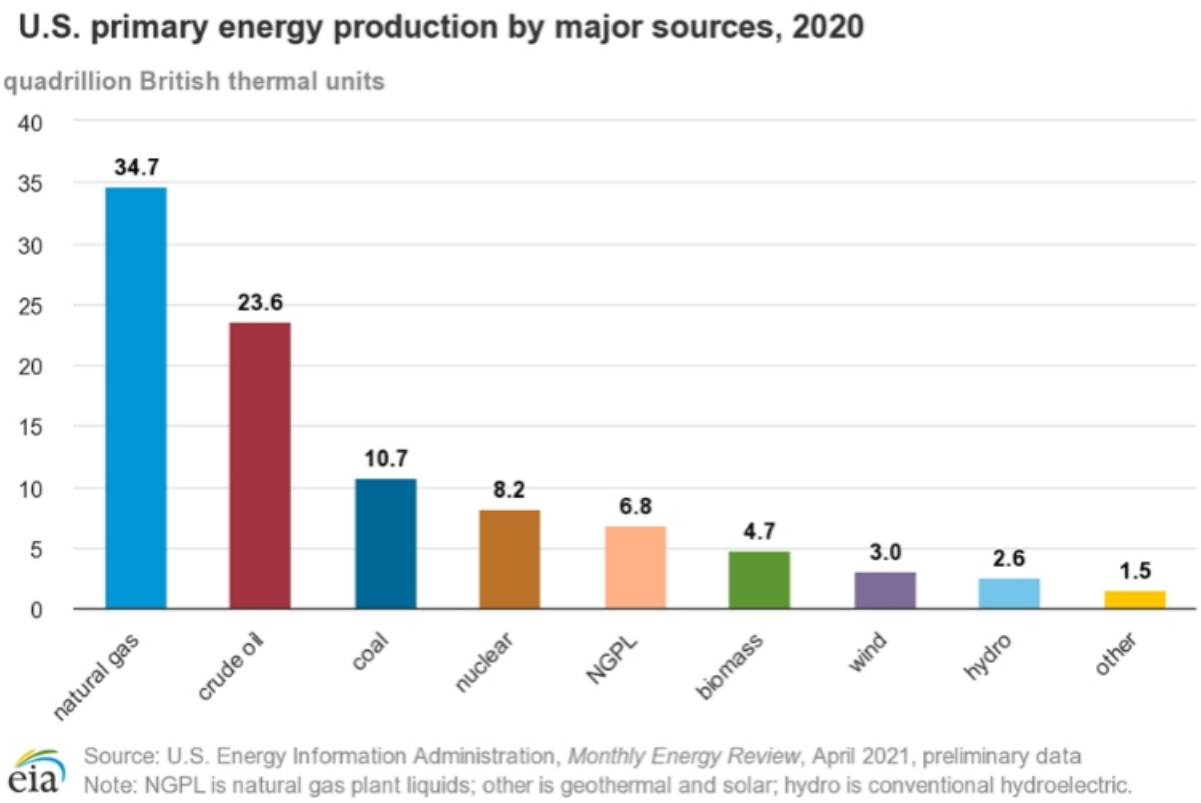

Figure 1. Energy production for primary sources in the US.[1]

Demand and consumption of energy are on the rise due to increased amenities, industries, and domestic consumption, among other consumers. Due to this increase, this critical resource is likely to be depleted with time. Besides its depletion, environmental issues are coming up in its use. Fossil fuels are the most produced in the US, as shown in Figure 1. These issues include the effects on climate, air pollution, and water pollution, among others.

Renewable energy is a promising route that can solve these climatic challenges by giving clean and environmentally friendly fuel. This renewable energy, however, has many other forms, such as solar energy, which are gradually increasing in demand and consumption. In addition to solar panels, hydrogen can be produced as a form of fuel. Hydrogen production can lead to a major source of energy generation even though molecular hydrogen does not freely exist in Nature.

And this, therefore, calls for more research to enable us to obtain clean and environmentally friendly energy.

This fact calls for more research that can be able to solve these environmental issues. In this regard, hydrogen production is a promising candidate for producing clean energy. Data indicates that the USA's renewable energy production has been on an upward trajectory with time, demonstrating that renewable energy is being embraced.[2]

1.2 Why hydrogen?

Hydrogen production as a fuel is a perfect replacement for fossil fuels. The ability of hydrogen oxidation to produce water as the only by-product gives about 140 kJg^{-1} of energy. On the other hand, gasoline generates 43 kJg^{-1} of energy and emits CO_2 as the by-product, a major environmental pollutant. [3] Based on this fact, hydrogen production is more attractive than fossil fuels which produce greenhouse gases that are more hazardous to the environment.

The production of hydrogen can better be achieved through research that can incorporate the use of renewable processes such as photoelectrochemistry for water splitting.

1.3 Photoelectrochemistry

Photoelectrochemistry, as shown in Figure 2, is a conventional process that involves converting solar energy through a photoelectrode that can exhibit the photovoltaic effect. This effect is brought about when light energy is converted to electrical power by semiconductors. This conversion takes place in the photovoltaic cell. The photovoltaic cell works on the principle that the semiconductor crystals absorb photons of light. The crystals acquire a steady state concentration of free electrons that can generously supply electrical current. [4]

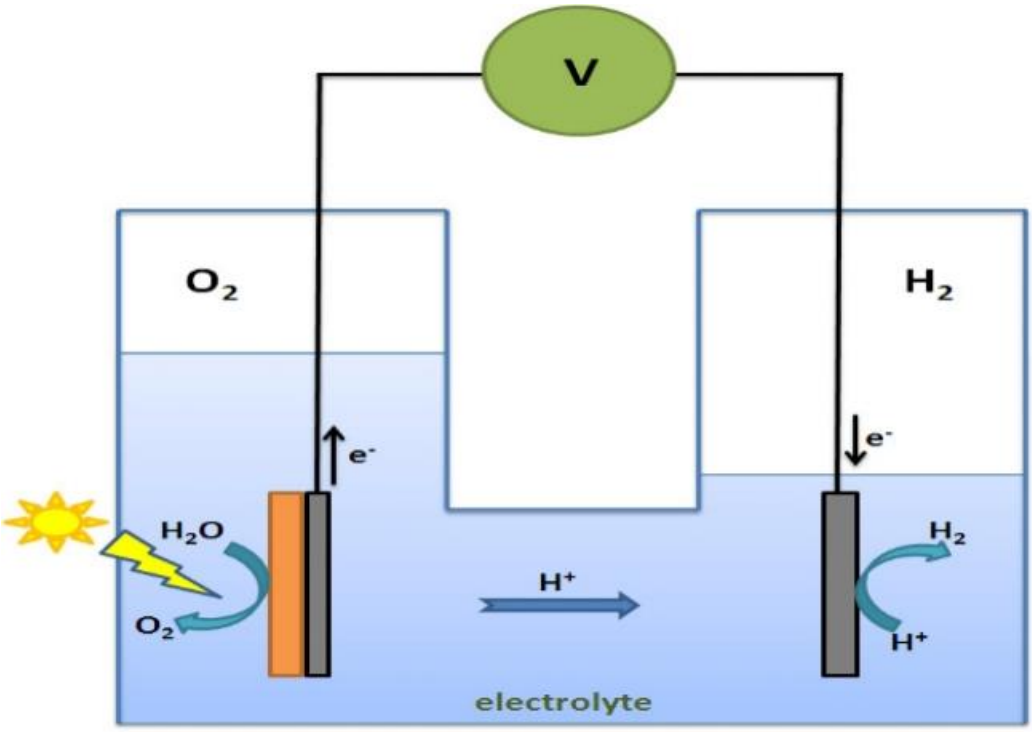

Figure 2**.** The schematic diagram for photoelectrochemistry. [5]

1.4 Photoelectrodes

Photoelectrodes are required for liquid junction photovoltaic cells, and these electrodes are made by fabricating semiconductive materials on a conductive surface. Therefore, for any material that someone uses in photoelectrode fabrication for solar photoelectrochemical water-splitting, it must have the following.

i. A band gap equal to or greater than 1.23 eV.

ii. High ability to withstand aqueous environments.

iii. Considerable photocorrosion resistance.

The conversion is majorly possible in the solar spectrum's visible region (400-800nm), where there is high intensity. Therefore the band gap should be around 2 eV, and WO_3 has a band gap of 2.6-2.8 eV to enable photosensitivity in this region.[6] It is worth noting that the valence band and conduction band edges should be higher and lower than water's oxidation and reduction potentials, respectively. These properties will give the photogenerated electrons and holes adequate energy to facilitate water-splitting. In addition, the photoelectrode is required to be more environmentally friendly for generating products and increasing efficiency.

1.5 Photoelectrochemical (PEC)cell

The water-splitting process is thermodynamically not easy to produce hydrogen and oxygen. A potential that is more negative than 0 V is required to reduce water in the water-splitting process, as can be seen in equation 2. Conversely,a more positive potential than 1.23 V is required to oxidize water, as shown in equation 1. The summation of these equations gives the overall water-splitting reaction, equation 3. These equations clearly show a minimum requirement of 1.23 V [7], equal to the Standard Gibbs free energy change ΔG^o of 237 kJ mol^{-1}.

$$2\ H_2O + 4\ h^+ \rightarrow 4\ H^+ + O_2 \qquad E_o\ Ox = 1.23\ V \qquad (1)$$

$$4\ H^+ + 4\ e^- \rightarrow 2\ H_2 \qquad E_o\ Red = 0\ V \qquad (2)$$

$$H_2O \rightarrow H_2 + \tfrac{1}{2}\ O_2 \qquad E_0 = 1.23\ V \quad \Delta G^o = 237\ kJ\ mol\text{-}1 \qquad (3)$$

This research used Pt wire as the cathode and the deposited WO_3 thin film samples as an n-type semiconductor photoanode.

Under sufficient irradiation of the photoelectrode, a semiconductor material, photons are absorbed with higher energies than its band gap. Due to the high energies, electrons in the valence band are excited and move to the conduction band, as shown in Figure 3; this action leads to the generation of excited electrons and holes in the conduction and valence bands, respectively. Through the help of an external bias, the electrons are moved to the cathode (Pt), where they are utilized to reduce water for hydrogen production. On the other hand, the holes in the valence band move from the photoanode (WO_3) to the electrolyte to oxidize water to give oxygen.

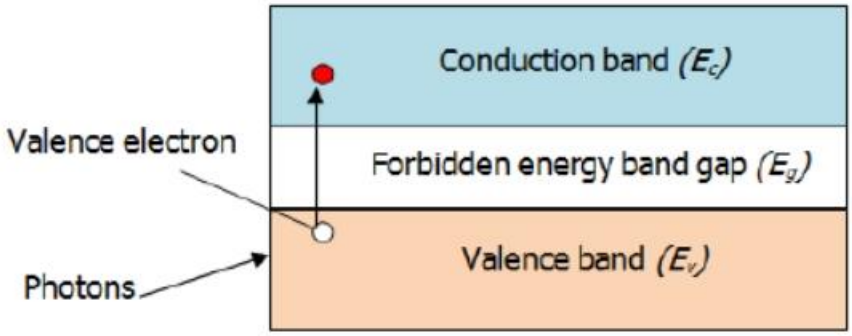

Figure 3. Movement of electrons from the valence band to the conduction band.[8]

1.6 Semiconductors operating principle

When a photoanode and an electrolyte come into contact, charge can be transferred between them. At the semiconductor-liquid junction interface, an electric field can be formed to strike a balance between the semiconductor and the electrolyte as can be seen in Figure 4. This action creates an identical electrochemical potential throughout the system, bringing about equilibrium.

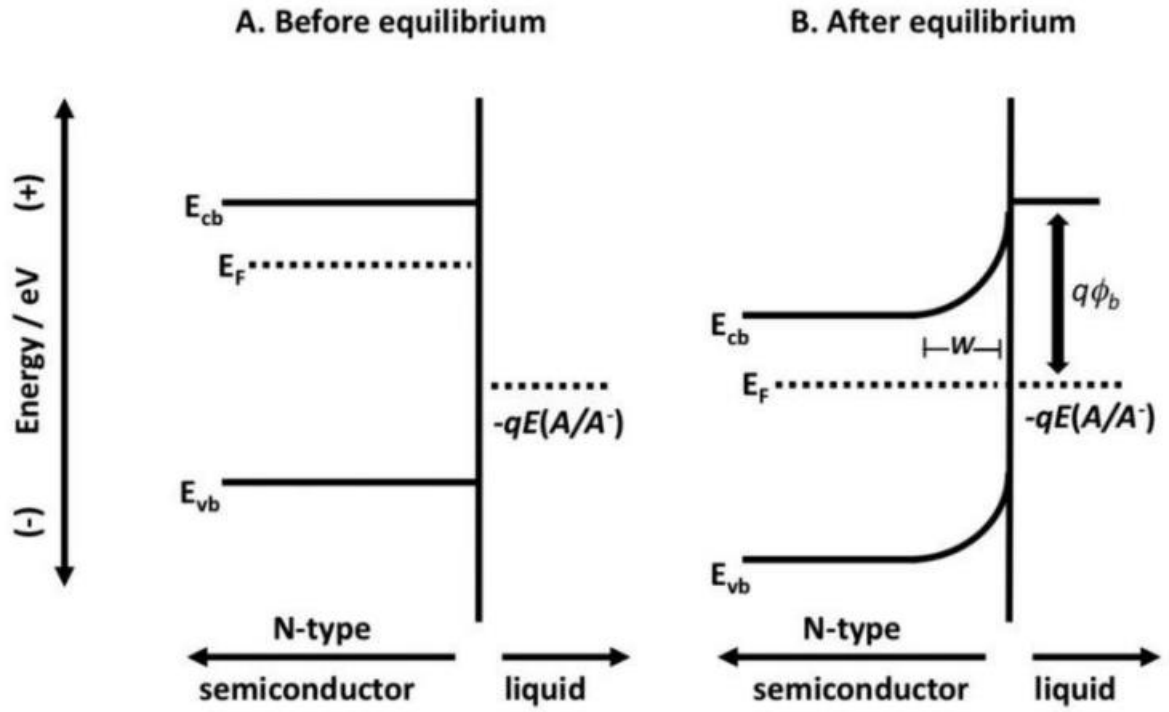

Figure 4. The band energetics of an n-type semiconductor-liquid contact in dark condition: (A) before equilibration, (B) after equilibration.[9]

For an n-type semiconductor photoanode, when immersed in a redox electrolyte, a couple of electrons are compelled to flow from the semiconductor into the electrolyte, creating an equilibrium state. After the equilibrium state is attained, the semiconductor photoanode will have a more positive charge due to the migration of electrons into the electrolyte. This leads to the electrolyte having more of a negative control. Since the charge carriers/electron densities are small in the semiconductor space charge region/depletion layer, the positive charge is spread over the depletion width of the semiconductors. In contrast, the negative charge will narrowly be spread in the electrolyte near the semiconductor.[10-13]

This phenomenon leads to the bending of the band edge as can be seen in Figure 5, which is caused by the drop in the electrical potential. The bending of the electric potential leads to the

separation of charge carriers in the semiconductor, in which holes(h+) move to lower electron potential. At the same time, the electrons(e) are attracted toward the bulk of the solid from the surface of the semiconductor. This explains why n-type semiconductors are naturally used as photoanodes to directly photo-generate holes through the electric field into the electrolyte solution.

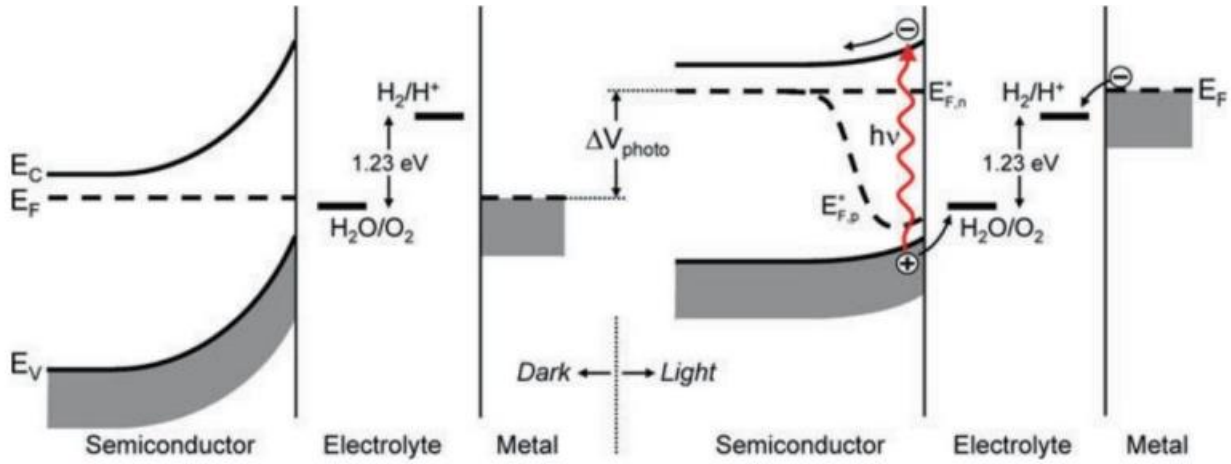

Figure 5. Band diagram for a PEC cell based on an n-type semiconductor photoanode which is electrically connected to a metal counter electrode: (left) in equilibrium in the dark condition; (right) under illumination.[10]

Irradiation of the semiconductor photoanode with photons whose energy is equivalent to or greater than the band gap minimum creates electron-hole pairs. Excess electrons hardly affect the majority carrier numbers, whereas the extra holes significantly change the minority carrier distribution concerning the equilibrium populations.

CHAPTER 2. LITERATURE REVIEW

2.1 Previous research

Extensive efforts have been made to investigate water's photoelectrolysis into H_2 and O_2. [14–16] Semiconductors play a crucial role in accomplishing this objective. Due to its high stability in acidic conditions and relatively small band gap (2.6 eV), tungsten oxide (WO_3) has attracted great interest in various research groups. [17–20] Photoelectrodes of WO_3 nanoparticles, nanoplates, nanowires, and nanorods have been fabricated on different conductive substrates. They have exhibited improved photoelectrochemical (PEC) activity, indicating the great potential of such WO_3 nanostructures. [21-34] WO_3 is an n-type semiconductor whose applications include gas sensing [35], electrochromic windows and displays,[36] catalyzes, [37] and photooxidation of water,[38-39] among others. Yamanaka[40] Et al. were the first to synthesize WO_3 thin films through cathodic electrodeposition. They prepared a precursor solution by mixing colloidal tungstic acid and concentrated hydrogen peroxide. Platinum was used to eliminate excess hydrogen peroxide. Unfortunately, their product could have been more stable since it underwent decomposition after some time. Further research was done to improve the stability of this precursor. Shen[41] et al in a study performed WO_3 deposition using different methods on indium-doped tin oxide (ITO) and fluorine tin oxide (FTO) substrates. Yang Et al.[42] used the sol-gel method to enhance the photoelectrochemical activity of tungsten oxide film through textural control. Jebet [43] fabricated WO_3 on stainless steel 304 thread through an electrodeposition process whereby the effect of pH on the precursor solution was investigated.

2.2 Fundamental properties of tungsten oxide (WO_3)

Also known as tungsten trioxide, tungsten oxide is an inorganic substance that is polymorphous. WO_3 appears as a light-yellow crystalline powder. It has a specific density of 7.16g/cm^3, melts at 1473 °C, and boils at 1750 °C. WO_3 sublimes at 850 °C and turns green when melted. Its solubility varies, insoluble in water and soluble in alkalis.

It exists in different forms, such as WO_3 and WO_2, among other binary oxides, such as $W_{18}O_{49}$, $W_{17}O_{47}$, $W_{20}O_{58}$, and $W_{40}O_{118}$. These oxides are non-stoichiometric, often expressed as WO_{3-x} ($0 < x < 0.3$). Due to their complexity, they have specific properties used in different studies.[44] WO_3 is the most common form of the oxides. Tungsten oxide has an oxidation state of +6.

Table 1. Summary on properties of tungsten oxide powder.

Compound Formula	WO_3
Appearance	Yellow-green powder
Melting point	1473 ^{0}C (2683F)
Boiling point	1750 ^{0}C (3092 F)
Density	7.16 g/cm^3
Solubility in water	insoluble
Crystal phase/structure	monoclinic
Exact mass	231.936 g/mol
Oxidation state	+6

Tungsten oxide is an n-type semiconductor with band gap energy ranging from 2.6 - 2.8 eV. Studies show that tungsten oxide can withstand different pH conditions and temperature conditions.[44]

The oxide of tungsten has been known since 1841, and since then, has been popularly known for its chromism, photocatalysis, and sensing applications, among other applications. Recent research [45]has focused on using tungsten oxide due to its semiconducting properties in developing a photovoltaic cell. Other metal oxides such as ZnO and TiO_2 have been used in solar cell technology, but have higher band gap energies, 3.37 and 3.2 eV, respectively. They can only utilize 5% of the solar spectrum, just the share represented by the ultraviolet region.

Variation in temperature affects the crystal structure of tungsten oxide. The monoclinic structure is the most predominant structure, which is known to have other crucial attributes such as photostability in acidic solution, excellent electron mobility, and long diffusion duration.[46] Figure 6 shows different structures of tungsten oxide.

As an n-type semiconductor, electrons, and holes are created in the conduction band (CB) and valence band (VB), respectively. The holes in the VB are energetic enough to oxidize H_2O to produce oxygen. However, the energy acquired at the CB does not have the equivalent ability to reduce hydronium ions to make H_2. Therefore, it cannot be proficient in completely decomposing water.[47] As temperatures increase, the oxygen vacancies increase in WO_3, leading to an increase in free electrons, the accumulation of these free electrons increases the energy which enhances water splitting.

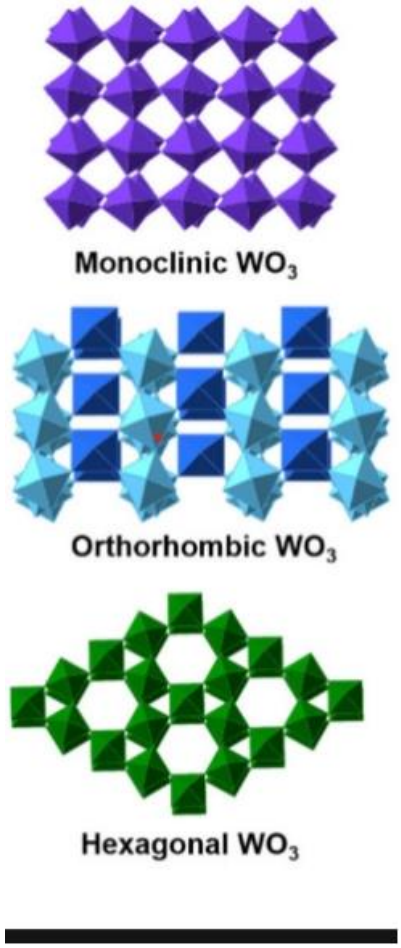

Figure 6. Crystal structures of tungsten oxide.[48]

2.3 Stainless Steel (SS) 304

This is an austenitic grade that majorly consists of iron-70%, chromium-18%, nickel-8%, and 2-% manganese. Other minor components include sulfur, silicon, and carbon.

2.4 Physical Properties of Stainless Steel 304

Table 2. Physical properties for 304 stainless steel alloys.

Property	**Value**
Density	8.00 g/cm^3
Melting Point	1450 °C
Electrical Resistivity	0.72 x 10^{-6} Ω.m
Thermal Conductivity	16.2 W/m.K
Thermal Expansion	17.2 x 10^{-6}/K

2.5 Passivation of stainless steel

Stainless steel can naturally self-passivate when its surface is exposed to specific environmental conditions by forming chromium oxide, which has good corrosion resistance. Chromium has a robust affinity for oxygen, which can promote the formation of this stable compound. The oxide formed can suppress further corrosion reactions. When the surface steel is thoroughly cleaned and free of contaminants, it can passivate, but passivation may also not happen when the surface is not cleaned. Nitric acid can remove light surface iron contaminants and promote the passivation of the surface of stainless steel. In addition, exposure to chromium on the surface of steel leads to the build-up of a chromium oxide layer which is impermeable and firmly adheres to the alloy's substrate. This leads to the formation of a protective coating.

However, the protective layer must be homogenous for the protection to be fully achieved. Any deviation from this will trigger the corrosion process due to generating different electrochemical potentials.[49]

2.6 Sol-gel method

Sol-gel process is a wet chemical technique that has been widely studied. Materials science is of great importance in the contemporary world, and sol-gel processing plays a crucial role in this science. The basic idea here is that a precursor solution is prepared, and this solution forms a web gel structure of distinct particles. In this precursor solution, gelation mechanisms (inorganic-polymerization) occur in which various forms of hydration and polycondensation alter the solution into solid oxide networks with unique properties. The particles formed have differences in morphology, crystallinity, and porosity, among other properties. The sol-gel formed can be dip-coated, spun, drop-cast, or doctor-bladed onto the desired substrates, including a thin film deposition**.** Most sol-gel process produces hydrated WO_3, which needs post-annealing treatment to obtain the crystallized form of WO_3. Figure 7 shows the sol-gel process employed in this research, starting from the precursor to sol to the right and ending at the film xerogel.

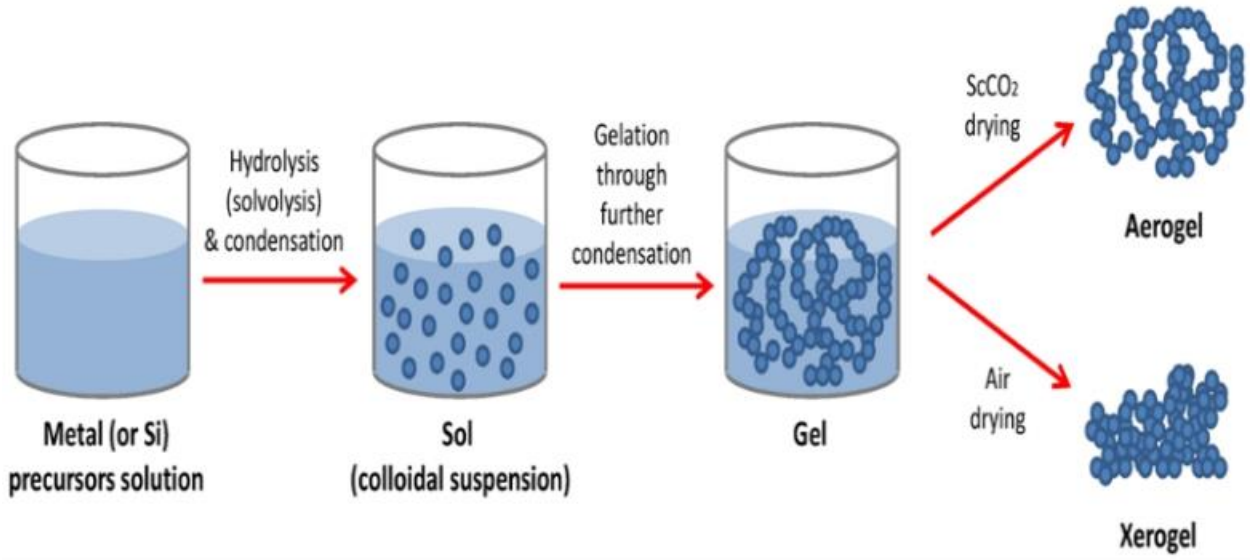

Figure 7. Diagram showing the steps in the sol-gel process.[50]

Different types of precursor solutions can be used to perform WO_3 sol-gel synthesis, but most studies have used aqueous solutions of tungstic acid and peroxotungstic acid solutions. In this research, peroxotungstic acid (PTA) was prepared as the precursor solution. Acidifying aqueous sodium tungstate solutions gives an aqueous solution of tungstic acid, whereas dissolving of tungsten metal in 30% H_2O_2 solution gives peroxotungstic acid.[51] The various morphologies of WO_3 can be attained during the sol-gel process through the control of precursor preparation and gelation process. The sol-gel process has the following merits and demerits.

2.6.1 Advantages of the sol-gel method [52-53]

- It is a less expensive technique.
- It can be done at low temperatures.
- It doesn't pollute the environment.
- Ability to create fine powders.

- Its chemical homogeneity is high.
- It is easy to control the size and the morphology of the particles formed.
- Chemical and physical properties of the dopants can be maintained in the case of doped sol-gel material.

2.6.2 Disadvantages of the sol-gel method

- The gel tends to shrink upon drying due to stress.
- The sol has a short life span.
- It is only possible to achieve a greater than 100 μm coating if organic components are added.
- It has an extended processing time.

2.7 Doctor-blade method

Doctor-blade is a technique for fabricating thin films on large surfaces.[54] This technique, illustrated in Figure 8, is a widely used method developed in the 1940s. For example, Howatt et al. [54] used this method to develop capacitors and thin sheets of piezoelectric materials. A well-mixed precursor consisting of nanopowders and other additives like binders, depressants, or plasticizers is made first during doctor-blading. The precursor is then spread on the substrate at a relatively constant movement between the blade and substrate to form a gel layer. The layer formed is later dried and annealed, which results in the formation of a thin film.

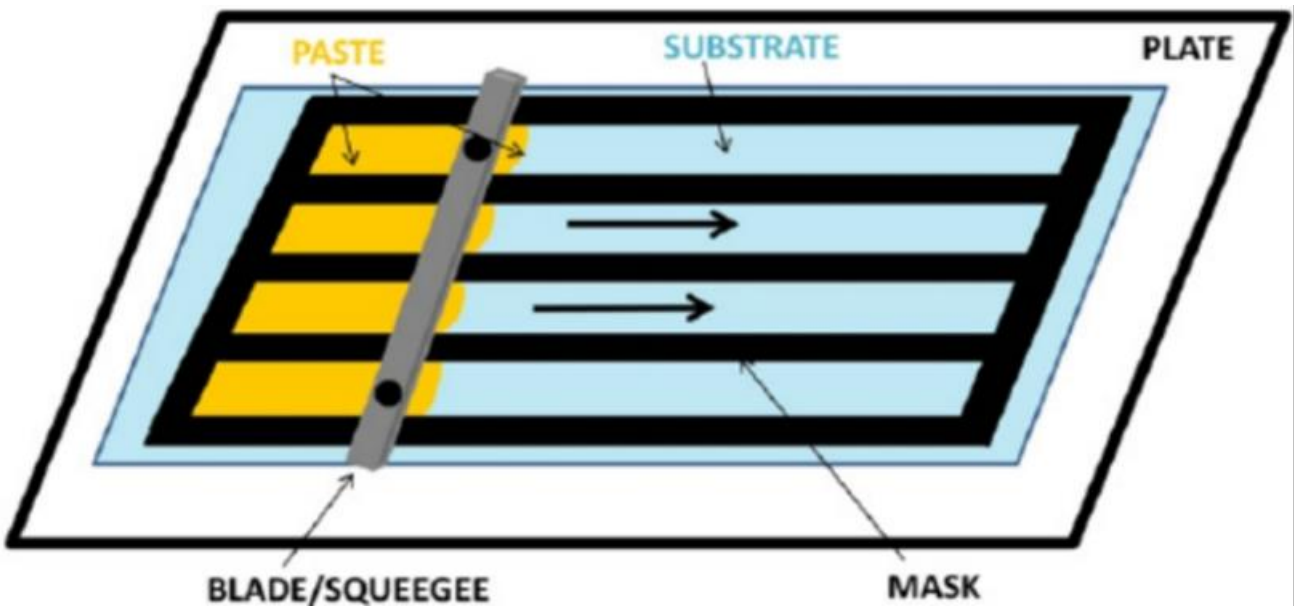

Figure 8. Schematic diagram of the doctor-blade method.[55]

2.8 Reaction Mechanism

Giannouli and Leftheriotis [56] give a description of the cathodic electrodeposition of WO_3 from peroxotungstic acid. This similar reaction was earlier reported by Yamanaka et al [40]. Dissolution of tungsten metal powder in 30% hydrogen peroxide leads to the formation of a predominant peroxotungstate dimer - $W_2O_{11}^{2-}$.

$$2\ W_{(s)} + 10\ H_2O_{2(l)} \rightarrow W_2O_{11}^{2-}{}_{(aq)} + 2\ H^+_{(aq)} + 9\ H_2O_{(l)}$$

In this case, the result indicated that the solution's nature is highly acidic. The acidity of the solution is caused by the dimeric species. The formed peroxotungstates are unstable and therefore they decompose slowly. The decomposition leads to the formation of a tungsten trioxide precipitate, according to the reaction below.

$$W_2O_{11}^{2-}{}_{(aq)} + 2\ H^+_{(aq)} \rightarrow 2\ WO_{3(s)} + 2\ O_{2\ (g)} + H_2O_{(l)}$$

Due to the instability of the dimers, isopropanol was added to improve the stability of the precursor solution.[57]

2.9 Statement of the problem

Warmer weather and environmental pollution are becoming increasingly global hazards. This has led to a tough call for more research to mitigate this problem. Water-splitting using solar energy has been seen to be a promising route that will enhance clean energy production. In addition, a more environmentally friendly atmosphere can be attained by producing hydrogen as fuel since the dependence on fossil fuels will be avoided.

2.10 Objectives

The primary objective of this research is to deposit thin films of tungsten oxide on the surface of conductive stainless steel 304 substrates via sol-gel and evaluate the photoelectrochemical properties of the photoanode for water splitting. Despite numerous types of research about WO_3 as a semiconductor material, most have used FTO and ITO as conductive substrates for fabricating these photoanodes for solar water splitting. Despite its corrosion resistance, durability, photostability, and availability, less emphasis has been given to stainless steel 304 as a conductive substrate. There is a need to develop methods for producing WO_3 films having high crystallinity with good intra-particle contacts. This study reports a straightforward method for producing nanostructured WO_3 films through the sol-gel process. The effect of annealing temperature on the crystalline of WO_3 thin film and the influence of the cleaning reagents on the stainless-steel substrate are investigated.

2.11 Specific objectives are:

1. Deposit WO_3 sols on stainless steel substrates using the doctor-blading method and after forming a gel, anneal the samples at 200 °C - 500 °C and characterize using SEM and XRD to check the morphology and crystallinity.

2. To investigate the photoactivity of the samples through the photoelectrochemical linear sweep voltammetric technique.

3. To confirm the thickness and uniformity of the WO_3 thin film deposited on stainless steel substrate using profilometry.

2.12 Significance of the research

The use of various materials as substrates for WO_3 thin film deposition for solar applications has been exploited with some challenges, which include cost and reliability. Using the sol-gel method for depositing tungsten oxide thin films on stainless steel 304, more solar energy could be utilized to generate power since sol-gel can enhance large surface area applications. This concept can be very useful since it can lead to the reduction of overdependence on fossil fuels globally.

CHAPTER 3. EXPERIMENTAL AND INSTRUMENTATION

3.1 Precursor solution preparation

3 g of W powder was weighed and added to 60 ml of 30% H_20_2. The mixture was stirred for 6 h at room temperature in which a pale-yellow solution was formed. Excess H_2O_2 was decomposed by adding a piece of Pt metal into the solution. Fizzing was observed which stopped after some time, indicating that H_2O_2 was fully decomposed.50 ml of 2-propanol was added to the mixture to stabilize the solution. Doctor blading was employed for the deposition of the precursor solution/WO_3 thin layers on stainless steel 304. The film was left to dry for 30 minutes in air, and annealing was done at different temperatures between 200 ℃-500 ℃ at an increased temperature rate of 15 ℃ per minute for 1 hour.

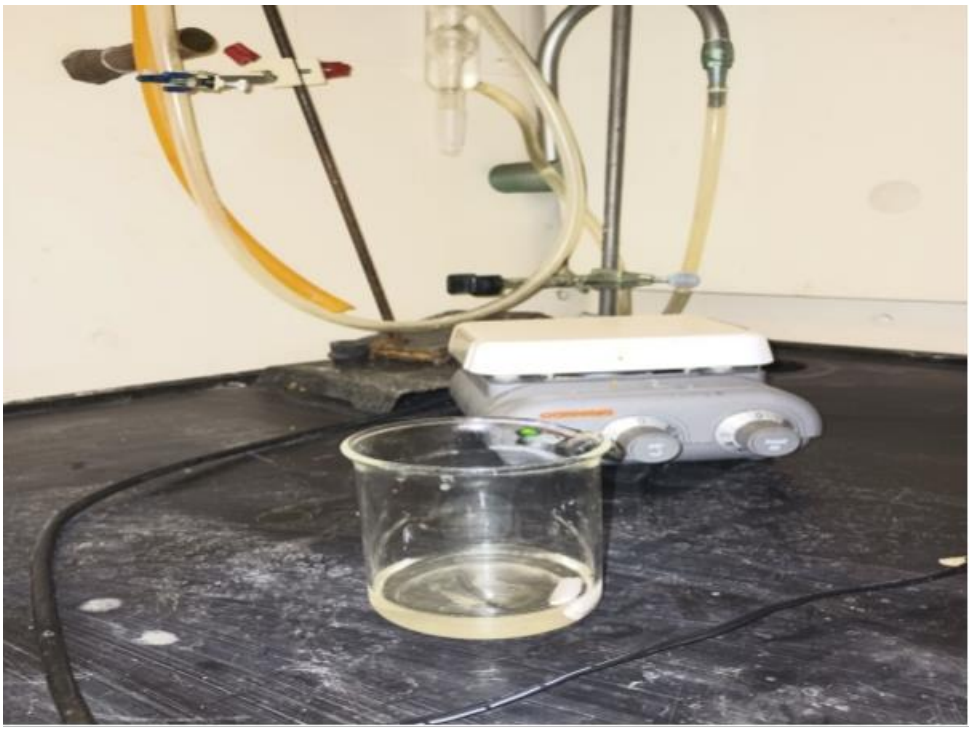

Figure 9. Pale yellow precursor solution of WO_3

3.2 Substrate cleaning procedure

For good film adherence on the stainless steel 304 and uniformity of the film, the substrate was thoroughly cleaned using the following procedure before deposition on the surface.

1. SS 304 was cleaned by ultrasonication in acetone for 5 minutes at room temperature. The cleaning was done to remove any glue or grease material on the surface of the substrate.
2. Substrate was washed in deionized water to eliminate any acetone.
3. The substrate was etched in 0.1 M HNO_3 and ultrasonicated for 30 minutes to remove any remaining contaminants and passivate our substrate.
4. Rinsing was again done using deionized water and this was to ensure that all HNO_3 was removed.
5. The substrate was then left to dry in air for 30 minutes before the deposition of the film.

To substantiate uniform deposition, uniform thickness, and consistent crystal forms of tungsten oxide on the SS304 substrate, the deposited films were characterized using scanning electron microscopy (SEM), X-ray diffraction (XRD), profilometry and cyclic/linear voltammetry.

3.3 X-ray Powder Diffraction (XRD)

This is an analytical technique that is usually used in the identification of phases of crystals. This technique helps in giving information on the cell units and the arrangement of atoms per given space.[58] This technique was discovered by Max Von Laue in 1912 whereby it works under the principle of constructive monochromatic X-ray interference. Monochromatic X-rays are majorly produced by cathode ray tubes in which they are filtered and directed towards the sample for

interaction. This interaction leads to the generation of diffracted rays.[58-59] In order to achieve constructive interference, the working conditions must satisfy Bragg's Law. This instrument consists of three major components: the X-ray tube, a sample holder, and an X-ray detector. The X-ray tube generates X-rays through the heating of a filament to release electrons. The produced electrons can be directed to the target material for interaction purposes through the application of a voltage. The target holder puts the target material in the correct orientation for interaction with the rays. The detector collects the X-ray signals, records them, and converts them as they are displayed on the computer screen as the output. [58]

Figure 10. Rigaku MiniFlex II XRD instrument at the YSU laboratory.

3.3.1 Strengths of X-ray Powder Diffraction (XRD)

- It is a fast technique for identifying an unknown mineral.
- It gives explicit mineral determination in most cases.
- Sample preparation for analysis is simple.
- XRD uses units that are readily available.
- It has simplified data interpretation.

3.3.2 Limitations of X-ray Powder Diffraction (XRD)

- Requires finely grounded material for analysis.
- It has a low detection limit of about 2% of the sample for mixed materials.
- It is complicated for pattern indexing in non-isometric crystal systems.

3.4 Scanning Electron Microscope (SEM)

This is a type of microscope in which an image is formed using electron beams instead of light. The technique was established in the early 1950s to increase the volume of examination of specimens. In this research the technique was used because it has a large depth of field, enables the focusing of more specimen area at a time, and its resolution is stronger, which enables magnifying tightly packed specimens, and can also give clear images. Through a vacuum inside the microscope, beams of electrons are directed from a gun in a vertical pathway onto the sample. This beam of electrons hits the sample to generate more electrons and X-rays. Electrons and X-rays are then collected by detectors where they are converted to signals, which present the

image on a screen for analysis.[60] Below in Figure 11 is a schematic diagram to illustrate how the beam of electrons moves to a sample.

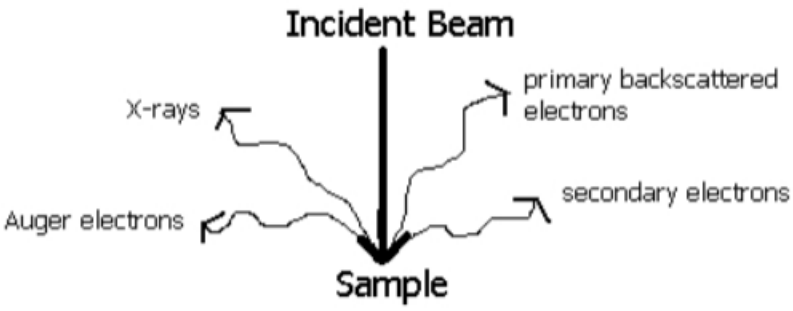

Figure 11**.** Diagram of various processes resulting from an incident electron beam.[60]

During sample testing, water was removed from the sample through drying to avoid vaporization taking place in the vacuum. It is worth noting that when we were carrying out the sample tests for ITO, which is a non-metallic glass substrate, the sample was grounded by covering a portion of ITO with conductive copper tape.

In this research, samples were sized into 2 cm x 2 cm and then mounted in the SEM-EDS chamber for analysis. The JEOL JIB-4500 apparatus was greatly useful in carrying out the SEM and EDS characterization.

3.5 Voltammetry

A potentiostat is useful in carrying out electrochemistry experiments in which various techniques are applied. In this research, cyclic voltammetry techniques and others were used whereby the redox reactions were investigated in the solution. In our technique, a three-electrode system was used, employing working, counter, and reference electrodes.

By using the potentiostat, the current between the working electrode and the counter electrode was measured and the potential between the working electrode and reference electrode was measured. This was done with the objective of investigating the redox potentials of materials, and the reversibility of the reactions among other properties of electrochemical reactions. In our research, the working electrode was the thin film of WO_3 deposited on stainless steel sheet where electrochemical reactions and transfer of electrons took place as current, and potentials were measured. In this research, the reference electrode was $Ag_{(s)}/AgCl$, which gave a stable potential in controlling and measuring the working electrode and counter electrode, whereas the counter electrode was Pt wire, which helped complete the system's circuit. The material that was used in making the counter was highly electroconductive.

Figure 12. Photo of the PAR potentiostat model 273A.

3.6 Profilometry

In this technique, the profilometer device was used to check the topographical nature of the sample by measuring the height of the uppermost layer. This device helps in giving a clear picture of the textural variation of the model being tested. This technique helps distinguish the physical properties of the samples we were testing. The results obtained from the sample tests reveal whether the materials have a distinctive directional lay. This will promote quality control of the products.

In this research, a surface contact profilometer with high-precision components for data acquisition was used to measure distinct features. The substrate was placed on a base plate, and

the sensitive stylus was adjusted to make physical contact with the sample. The stylus could record the variations in height on the surface of the sample as it was drawn across at a constant speed.[61] It is recommended that the scanning should start on a bare section of the substrate to observe the step height. This scan also helps in obtaining the precise values of the film thickness. In this study, the speed of 0.2 mm/sec, range of 100 microns, length of 5 mm, and stylus force of 10.0 mg was used to obtain the thickness of the film.

Figure 13. KLA Tencor D-100 stylus profilometer in YSU laboratory.

CHAPTER 4. RESULTS AND DISCUSSION

4.1 Stainless steel 304 compositions

Confirmation of the composition of the stainless steel 304 substrate was done through XRF characterization. The following photograph shows the substrates that were used in the analysis.

Figure 14. Photograph of stainless steel 304 substrates.

Table 3 shows the findings from the analysis of the major components. This result seemed not to have many discrepancies from the literature results in which 70% iron, 2% manganese,18% chromium, and 8% nickel.[49]

Table 3. Elemental XRF analysis for ss 304.

Fe	Mn	Cr	Ni
70.26%	1.51%	17.93%	7.34%

The XRD analysis of the substrates was done to confirm the crystal structure of the substrate. The characteristic peaks for stainless steel 304 in XRD analysis revealed that the substrate has a mixture of phases with 6 major peaks: γ (111), α (110), γ (200), α (200), γ (220), and α (211) at 2θ = 43.72, 45.3, 51.4, 74.8 and 82.4, respectively, as shown in Figure 15. These results are in line with the literature by Peng et al.[62]

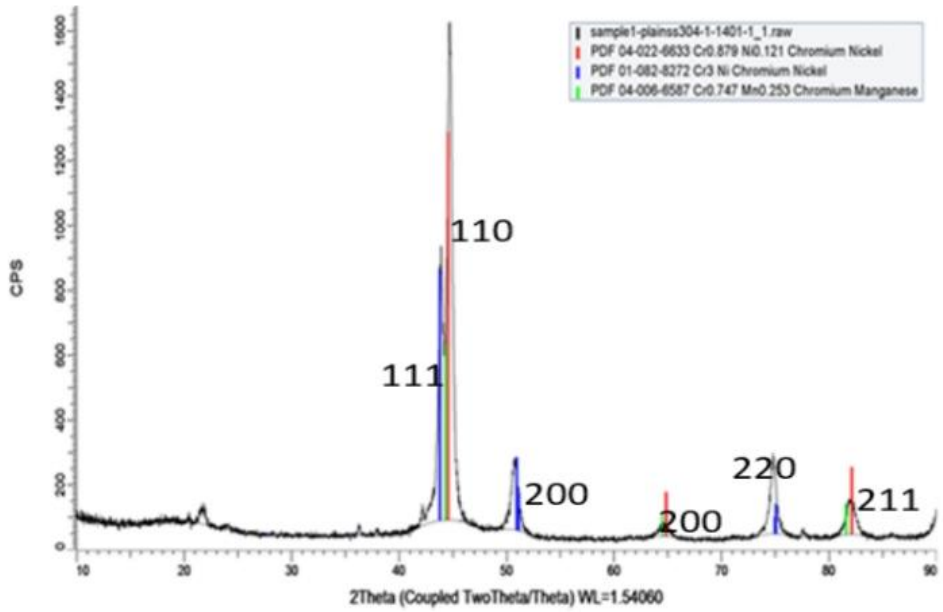

Figure 15. XRD pattern for plain stainless steel 304 substrate.

4.2 Effect of annealing temperature on stainless steel 304 substrate

Different samples of plain SS 304 substrate were annealed at different temperatures (200 °C, 300 °C, 400 °C, and 500 °C) to investigate the effect of heat on the substrate. Different photos that were taken indicated that as the annealing temperature increased, the stainless steel substrate became browner. This might have been caused by the oxidation of the surface layer of the

substrate to form an iron (III) oxide, which gave it a brown color. It was however established that the formation of brown color does not influence the substrate structure that may affect its performance. The XRD result indicated that all samples that were annealed at different temperatures (200 ℃ - 500 ℃,) showed similar peaks as the peaks of unannealed plain SS 304 of Figure 15 above. Figures 16(a-d) show the changes in the appearance of SS 304 annealed at different annealing temperatures.

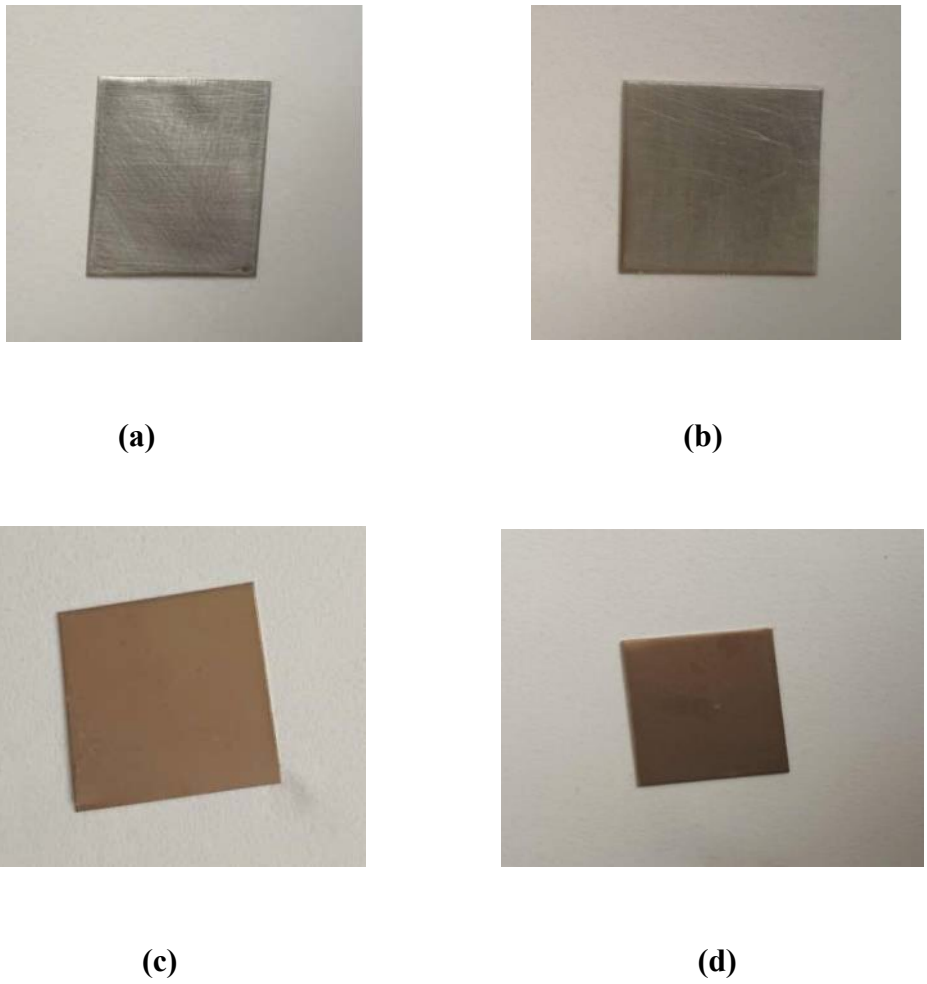

(a) **(b)**

(c) **(d)**

Figure 16. The photos16(a,b,c,d) shows the changes in the appearance of SS 304 annealed at different annealing temperatures (200 ℃, 300 ℃, 400 ℃, 500℃), respectively.

4.3 Cleaning procedure on SS 304 substrate

The effect of the cleaning reagents on the substrate was investigated to determine their effect on the structure of the substrate. Deionized water, acetone, and 0.1 M nitric acid were used as highlighted in the cleaning procedures in Chapter 3. It was revealed that acetone and deionized water did not have an effect on a stainless steel substrate. Figure 17(a) and (b) shows the change in the physical appearance of stainless steel after the substrate was first cleaned in deionized water and then cleaned in acetone compared to the substrate immersed and ultrasonicated for 30 minutes in 0.1 M HNO_3(Figure17 b), which shows the substrate to be shinier than in Figure 17(a), an indication that the treatment of the substrate in HNO_3 influences the surface.

17(a)

17(b)

Figure17. (a) photograph showing the substrate which was not treated in 0.1 M HNO_3 and (b) a shiny surface of a substrate after being immersed and ultrasonicated for 30 minutes in 0.1 M HNO_3.

4.4 XRD characterization for SS 304 substrate cleaning procedure

XRD analysis was done on a stainless-steel substrate after each cleaning agent was used to establish the effect on the substrate. In this section, the samples cleaned with deionized water and acetone did not have a noticeable effect on the substrate. The same peaks as those of plain stainless steel 304 were identified as γ (111), α (110), γ (200), α (200), γ (220), and α (211). When 0.1M of nitric acid was used in treating the sample as described in the cleaning procedure, extra peaks (002) and (110) were formed at around 2θ = 36.5 and 2θ = 38.5, respectively, as shown in Figure 18. These peaks correspond to chromium oxide peaks which are very crucial in promoting the corrosion resistance of the substrate. This is due to the passivation process enhanced by nitric acid treatment on stainless steel 304 substrate. These findings correlate with the literature.[49]

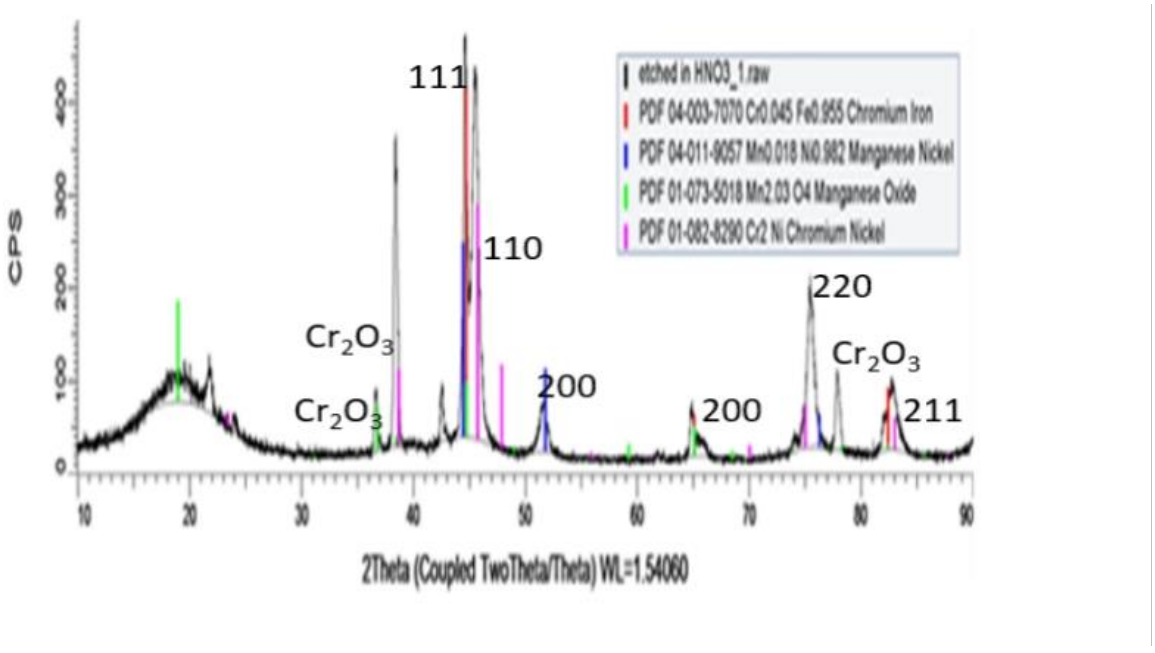

Figure 18. XRD pattern for stainless steel 304 substrate immersed and ultrasonicated for 30 minutes in 0.1 M HNO_3.

4.5 Deposition and Characterization of tungsten oxide thin film on SS 304 substrate

The precursor solution was prepared as indicated in Chapter 3 and then by using doctor blading, it was deposited on the surface after the substrate cleaning procedures had been thoroughly followed. The photograph in Figure 19(a) shows the sample of plain stainless steel 304 substrates before deposition. The sample in Figure 19(b) shows the as-deposited(not annealed) sample after drying it in the air for 1 hour. There is a noticeable difference in appearance between the plain SS 304 and the as-deposited WO_3 film, which clearly shows that the film was deposited.

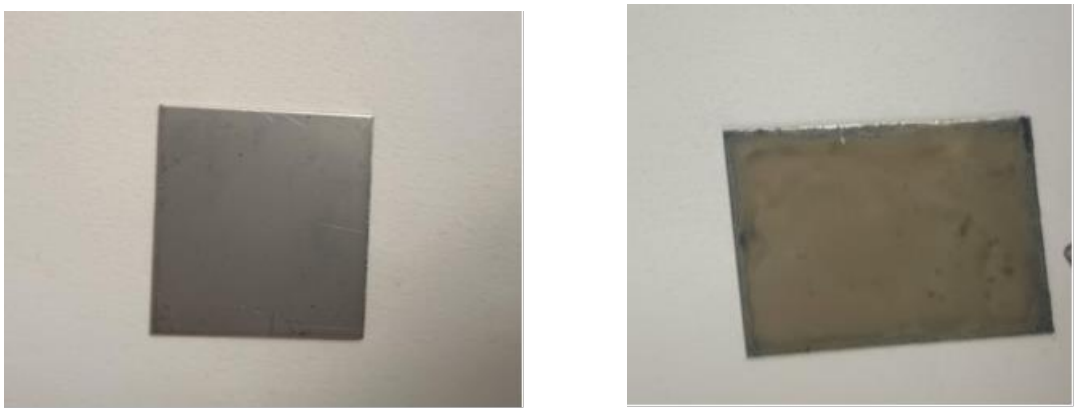

(a) (b)

Figure 19. (a) Photograph showing the stainless-steel 304 substrate before depositing WO_3 thin film and Figure 19(b) shows a pale yellow as-deposited WO_3 thin film on the substrate after drying in the air for 1 hour.

4.6 SEM/EDS Characterization of the deposited WO_3 thin film on SS 304 substrate

A plain steel substrate was characterized before the WO_3 film was deposited to act as the control. This was done by SEM measurement and the results are shown in Figure 20(a). These results between Figure 20(a) and Figure 20(b) clearly indicate the morphological difference between plain stainless steel and the as-deposited WO_3 thin film sample (no annealing). The WO_3 film sample in Figure 20(b), shows morphological features which are not seen on the stainless steel 304 substrate in Figure 20 (a). The results in Figure 20(c) clearly indicate the presence of W and O elements, an indication that the WO_3 film was deposited on the surface of the substrate. The intensity of the Fe peak decreased as compared to the intensity of W in Figure 20(c) and this is proof of the deposition of WO_3 thin film on the substrate.

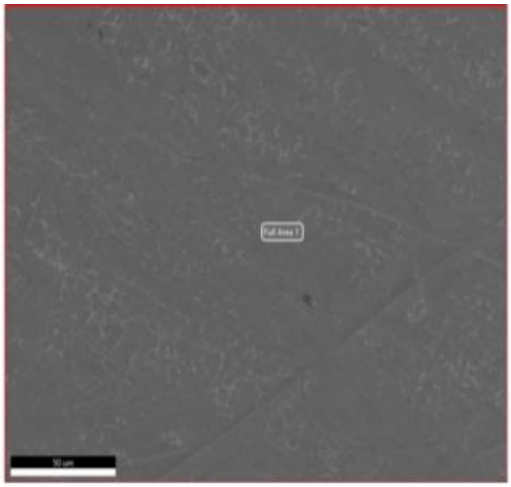

(a)

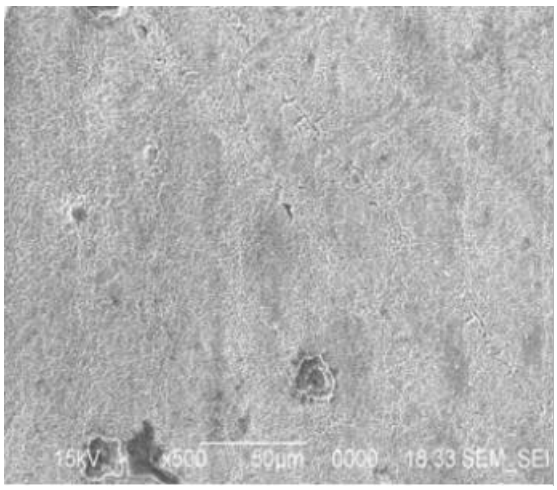

(b)

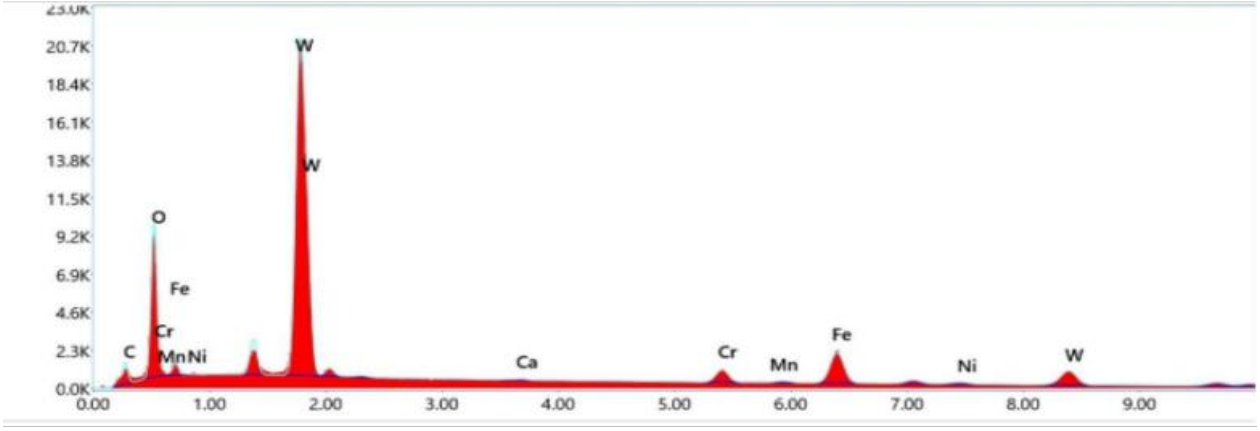

(c)

Figure 20. a) SEM for plain SS 304 substrate(b) as-deposited WO_3 film on SS 304(c) EDS for the as-deposited WO_3 on stainless steel 304.

Table 4. EDS analysis for the as-deposited WO_3 on SS 304.

Element	Weight %	Atomic %
C	11.96	33.74
O	21.48	45.48
Cr	4.12	2.69
Mn	0.011	0.001
Fe	15.31	9.29
Ni	0.032	0.001
W	46.96	8.65

4.7 Electrochromic effect of WO_3 film on SS 304

Electrochromism is the property of a substance where it changes color when under the influence of an electric field. The material under study undergoes electrochemical reduction and oxidation. In this research, 0.1 M H_2SO_4 was used as an electrolyte. Cyclic voltammetric experiments were done at a voltage range of -1.0 V to +1.0 V in which the WO_3 thin film was used as the working electrode. A plain stainless-steel substrate (Figure 21) was used as the control and comparison with WO_3 samples annealed at 200 ℃ (Figure 22), 400 ℃ (Figure 23), and 500 ℃ (Figure 24). It was revealed from the result in Figure 21 that there was activity recorded due to hydrogen evolution which might have been caused by the absorption of hydrogen atoms by nickel in the substrate, whereas for WO_3 at 200 ℃ (Figure 22), there was a slight activity for oxygen evolution which is a counter-reaction to hydrogen evolution. At 200 ℃, the amount of heat was not sufficient to form an adherent film, or it completely converted the acid to oxide, so some of the peroxotungstic acid that was on the surface of the substrate dissolved into the electrolyte. The dissolution led to a decrease in WO_3 coverage and ion current, hence causing a faint blue WO_3 film, but still partially inhibiting H_2 evolution from the steel substrate. The film that was

annealed at 400 ℃ revealed relatively more electrochromic reversibility, which might have been enabled by swift H^+ ion movement into and out of the WO_3 film. In that regard, there is a cathodic wave seen that could probably represent the film turning blue due to the insertion of electrons counterbalanced by H^+ ions. On the other hand, the anodic wave represents the release of electrons to the steel substrate and H^+ ions to the electrolyte, causing the film to turn light yellow.

As the temperature was increased to 500 ℃, the ion current reached its lowest rate. The increase in temperature might have affected the permeability of H^+ ions. These findings point out that there is no need for annealing the WO_3 samples at elevated temperatures for electrochromic investigation. These findings are consistent with the work of Sharbatdaran et al.[63] It is worth noting that for better electrochromic results, additives can be added to the electrolyte to improve the sensitivity of the sample.

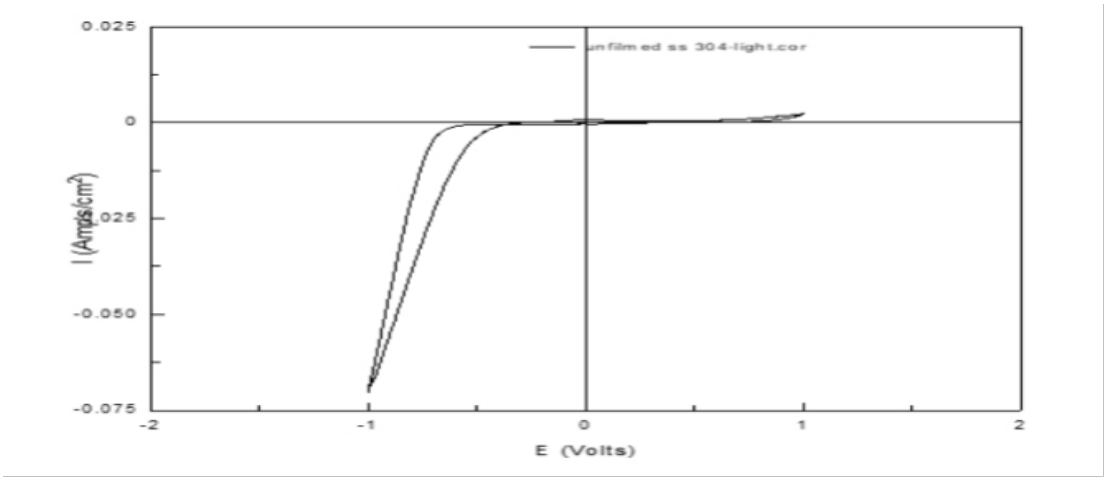

Figure 21. Cyclic voltammogram for plain stainless steel scan at 5 mV/sec, Pt wire, Ag/AgCl, and 0.1 M H_2SO_4.

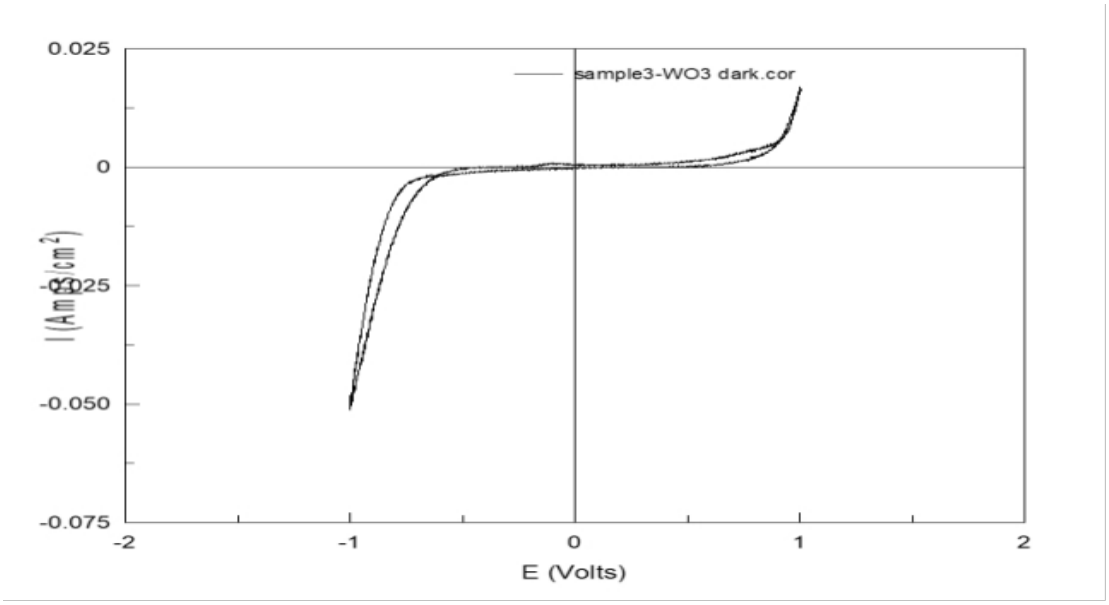

Figure 22. Cyclic voltammogram for WO_3 film sample annealed at 200 ℃ at a scan rate of 5 mV/sec, Pt wire, Ag/AgCl, and 0.1 M H_2SO_4.

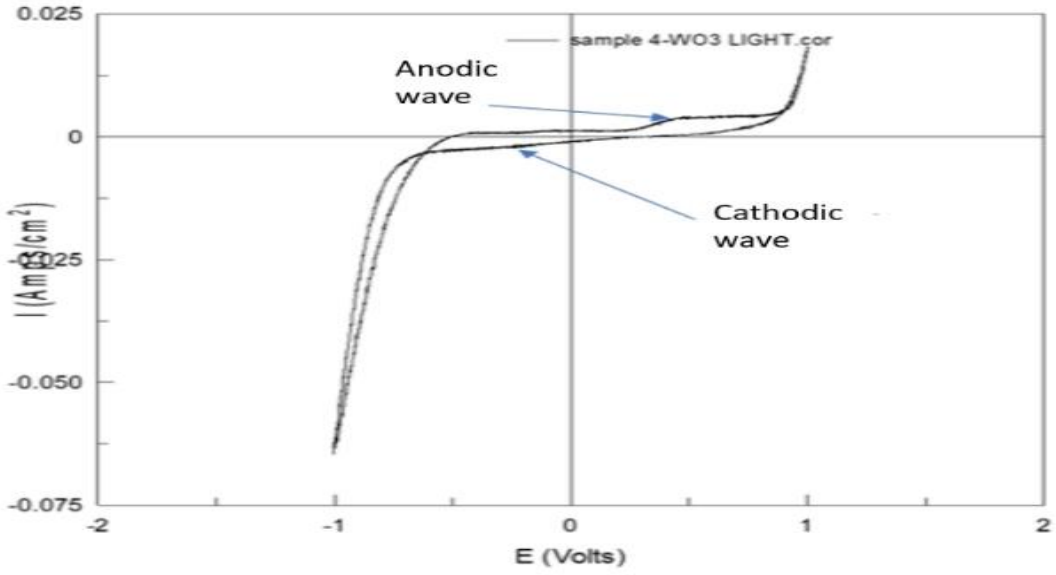

Figure 23. Cyclic voltammogram for WO_3 film sample annealed at 400 ℃ scan rate of 5 mV/sec, Pt wire, Ag/AgCl, and 0.1 M H_2SO_4.

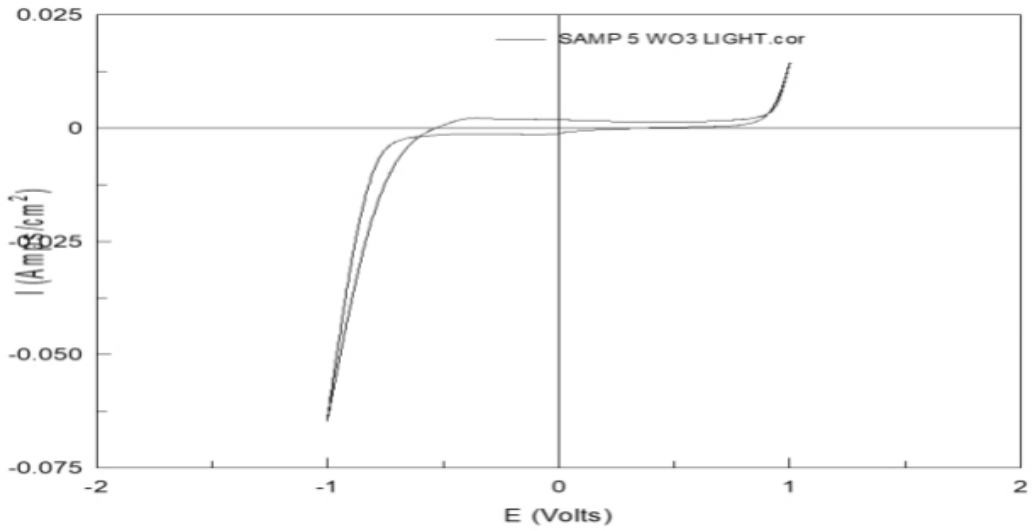

Figure 24. Cyclic voltammogram for WO_3 film sample annealed at 500 ℃ scan rate of 5 mV/sec, Pt wire, Ag/AgCl, and 0.1 M H_2SO_4.

4.8 The film thickness of WO_3 on SS 304 using a stylus profilometer

The thickness of the film influences the electrical, mechanical, optical properties, and the charge transfer of a particular material. Thin films contain several grain boundaries that can increase the scattered charge carriers. From the profilometry technique, the following results were obtained from samples annealed at different temperatures (200 ℃,300 ℃,400 ℃, and 500 ℃) as shown below. The film thickness measured by a profilometer was about 8, 6, 5, and 3.5 microns for the films deposited at different annealing temperatures, respectively. In comparing the uniformity of WO_3 film, the films obtained from annealing temperatures of 400 ℃ and 500 ℃ had relatively uniform thickness as compared to those that were annealed at 200 ℃ and 300 ℃.

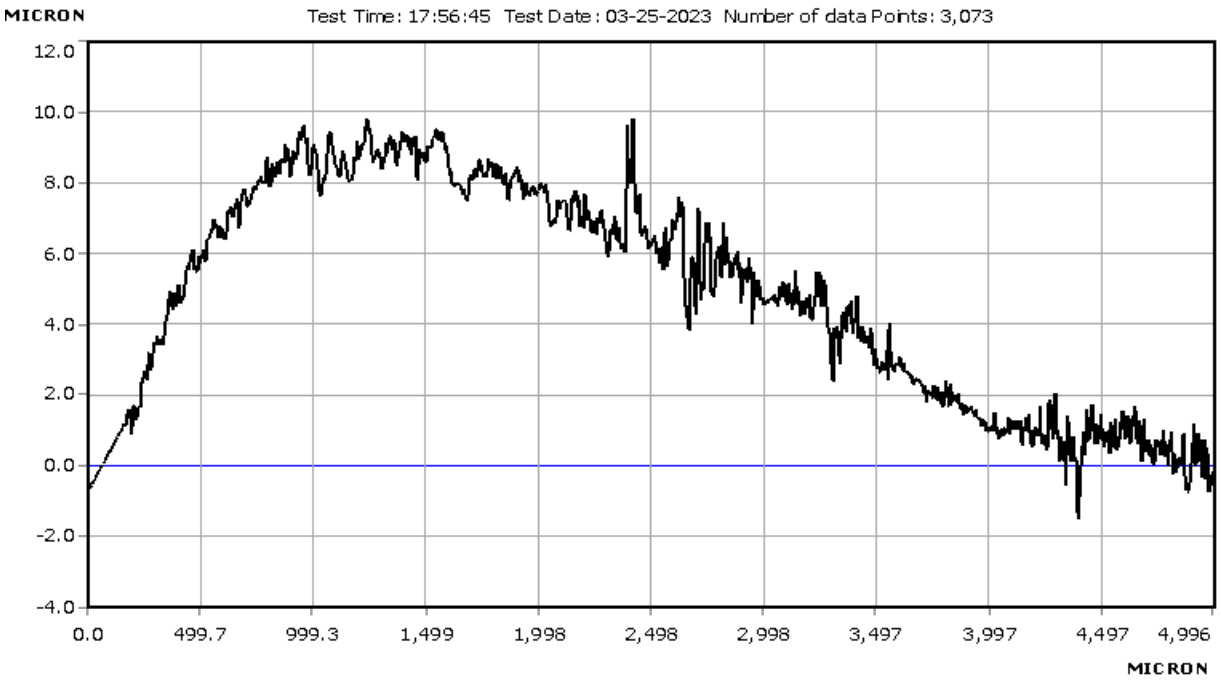

Figure 25. Profilometry measurement of WO_3 film annealed at 200 ℃ for 1h.

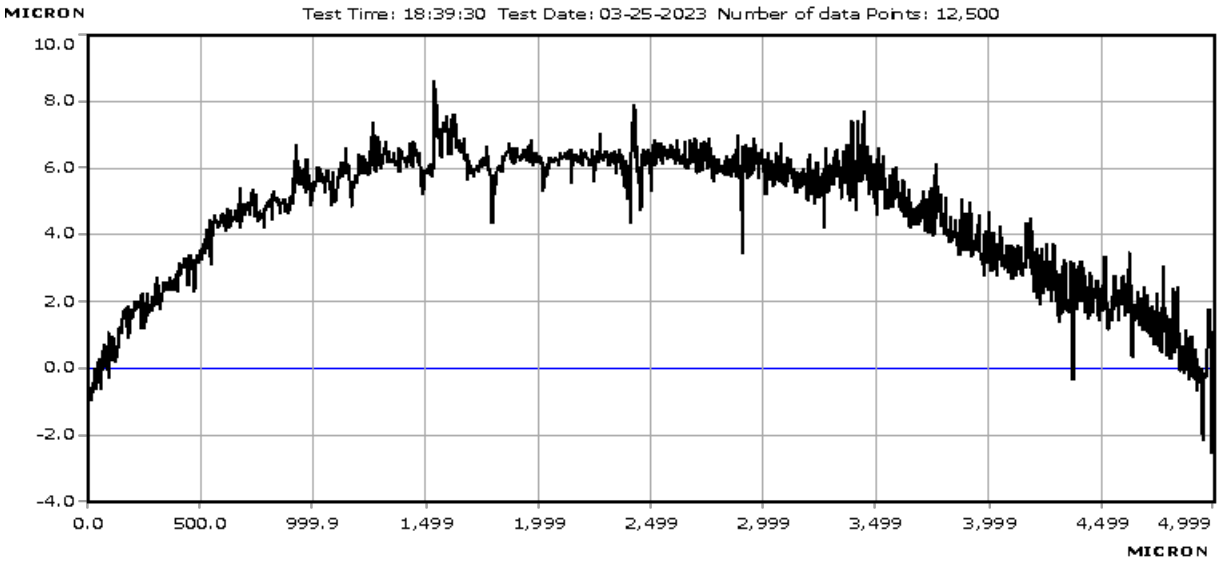

Figure 26. Profilometry of WO_3 film annealed at 300 ℃ for 1h.

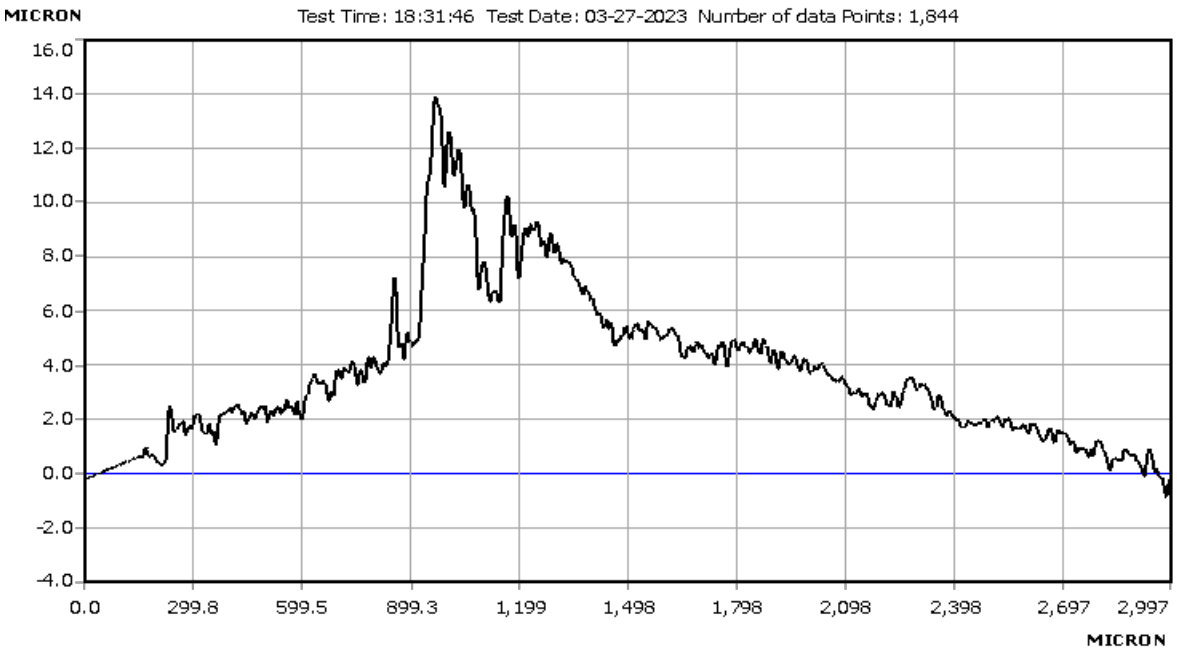

Figure 27. Profilometry of WO_3 film annealed at 400 ℃ for 1h.

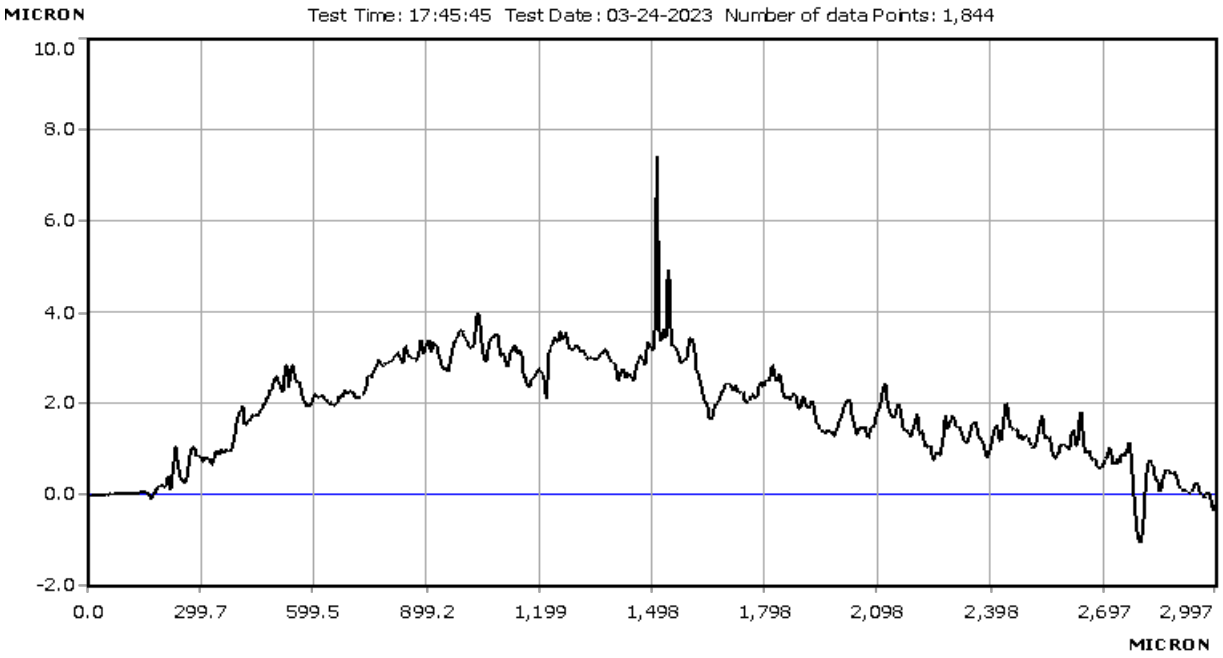

Figure 28. Profilometry of WO_3 film annealed at 500 ℃ for 1h.

4.9 SEM for the film thickness of WO_3 thin film on SS 304 annealed at 400 ℃ for 1h

Both SEM and stylus profilometer had nearly identical results on the thickness of the film in which SEM (Figure 29) showed a result of 5.127 microns whereas the profilometer(Figure 27) had about 5 microns.

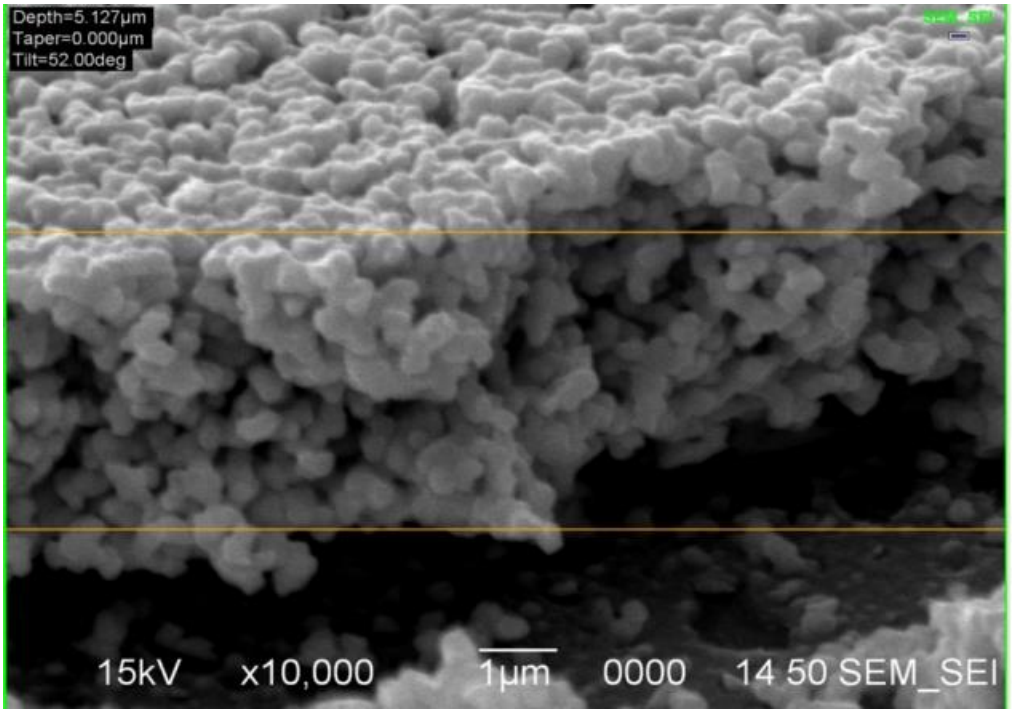

Figure 29. SEM photo for the film thickness of WO_3 film annealed at 400 ℃ for 1h.

4.10 Effect of annealing temperature on deposited WO_3 thin film on SS 304

All the annealing of samples was done in the air for one hour, and the temperature change rate was 15 ℃ per minute as the temperature was adjusted accordingly.

4.10.1 (a) Physical appearance of the annealed WO_3 thin films

On annealing WO_3 thin film samples at different temperatures, it was established that the physical appearance changed with the change in the annealing temperatures. It is evident from

Figures 30(a-d) below that the films that were annealed at 200 ℃ (Figure 30a) and 300 ℃ (Figure 30b) were more transparent due to their amorphous state. Studies show that in the amorphous state of a material, electrons are more localized around the oxygen vacancies, making them move to the closest tungsten sites; this affects the tungsten state and forms polarons there .[66] Film annealed at 400 ℃ (Figure 30c) had more monoclinic character than the films annealed at 500 ℃ (Figure 30d) . This made the film at 400℃ have a canary yellow color since WO_3 at 400 ℃ is more stoichiometric than at 500 ℃. This may be attributed to the oxide's crystallinity, which is more crystalline for the monoclinic phase. This changes the electronic density of states in tungsten and the electronic conductivity.[66]

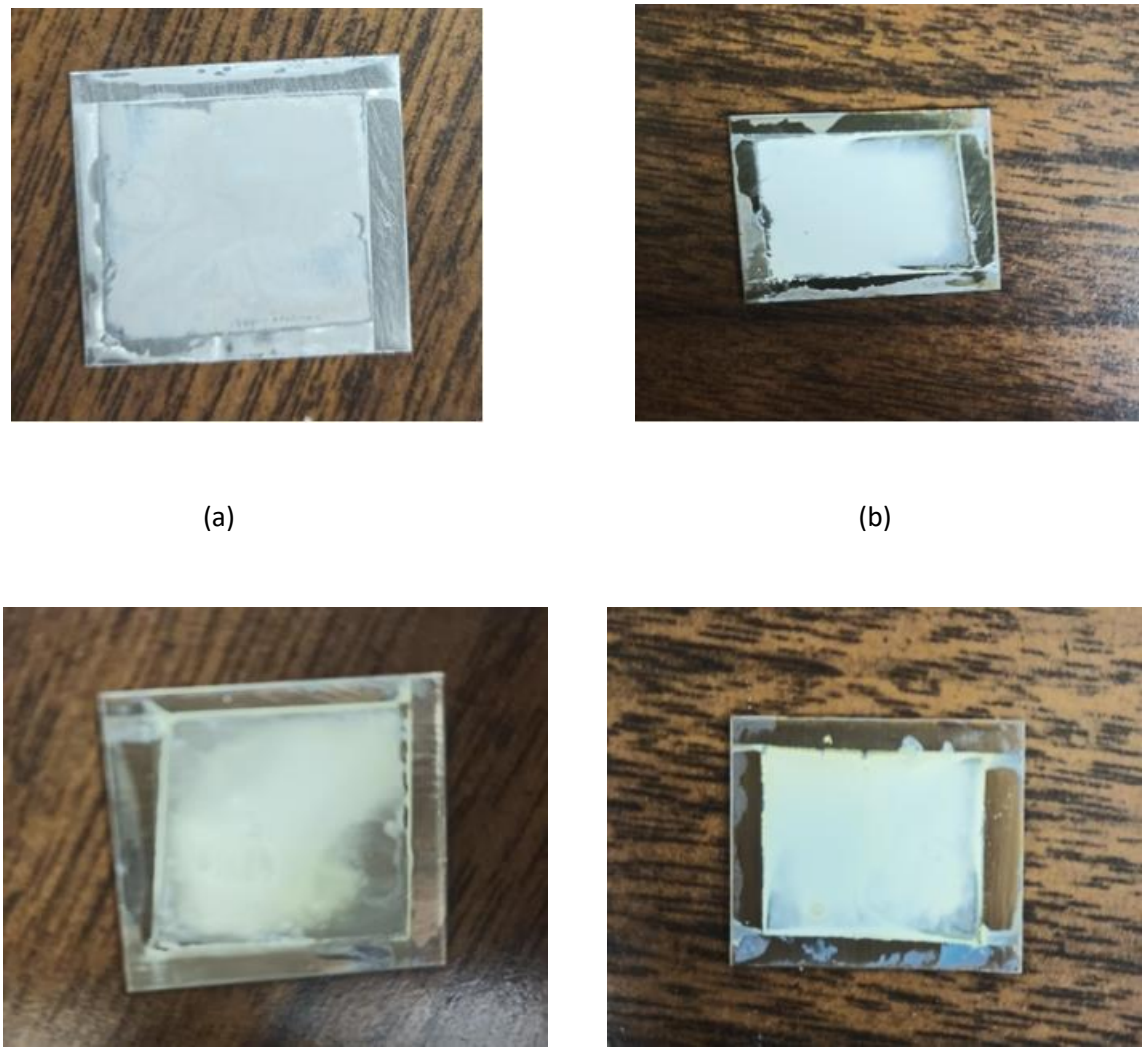

(a) (b)

(c) (d)

Figure 30. Photos (a,b,c,d) showing the changes in the physical appearance of WO_3 thin film annealed at different temperatures (200 ℃, 300 ℃, 400 ℃, 500 ℃) respectively.

4.10.2 (b) X-RD characterization of deposited WO_3 thin films at different annealing temperatures

Samples were analyzed by XRD in which the as-deposited sample was the control (Figure 31)**.** The XRD patterns revealed that the as-deposited sample and samples annealed at low

temperatures of 200 ℃ (Figure 32) and 300 ℃ (Figure 33) showed the amorphous nature of WO_3 films. This might have been attributed to the existence of water of hydration in the samples that made the structure of the samples remain semicrystalline. At 400 ℃ (Figure 34) the diffraction peaks reveal that the amorphous phase might have been transformed into a monoclinic structure. The structure showed a sharp orientation with high intensity. At this temperature, the water of hydration might have been vaporized, which enabled a better organization of the crystal structure. At 400 ℃ the sample might have received adequate energy that enabled the structure to arrange itself into a different phase most likely a monoclinic structure as seen between $2\theta = 23.4$ and $2\theta = 26.7$. This agrees with the findings of Memar et al [65]**.** It is worth noting that the good orientation seen must have been caused by the movement of the atoms with respect to the surface of the substrate, which is the lowest energy nucleation site that enhanced the best growth of the structures. This observation is in line with the literature by Yang et al.[42] At 500 ℃ (Figure 35) few peaks were observed, and these demonstrate that the monoclinic structures of WO_3 must have been converted to a different phase.

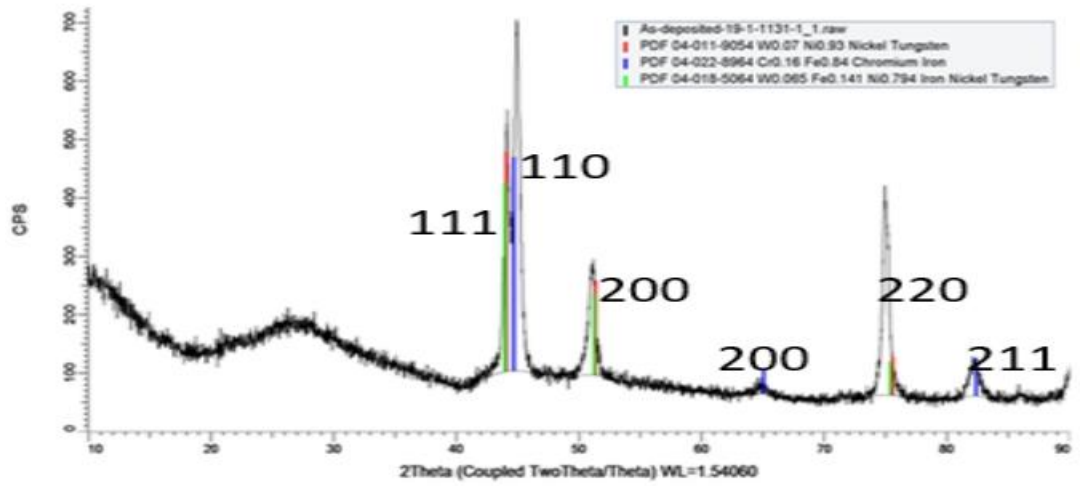

Figure 31. XRD pattern for as-deposited WO_3 thin film on stainless steel 304 substrate.

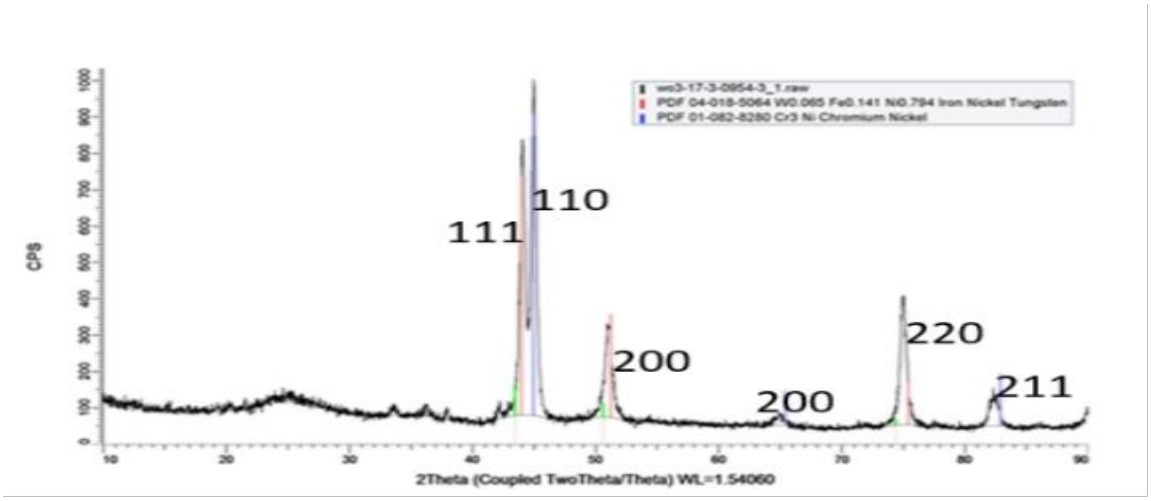

Figure 32. XRD pattern for WO_3 film sample on stainless steel 304 substrate after annealing at 200 ℃ for 1 h.

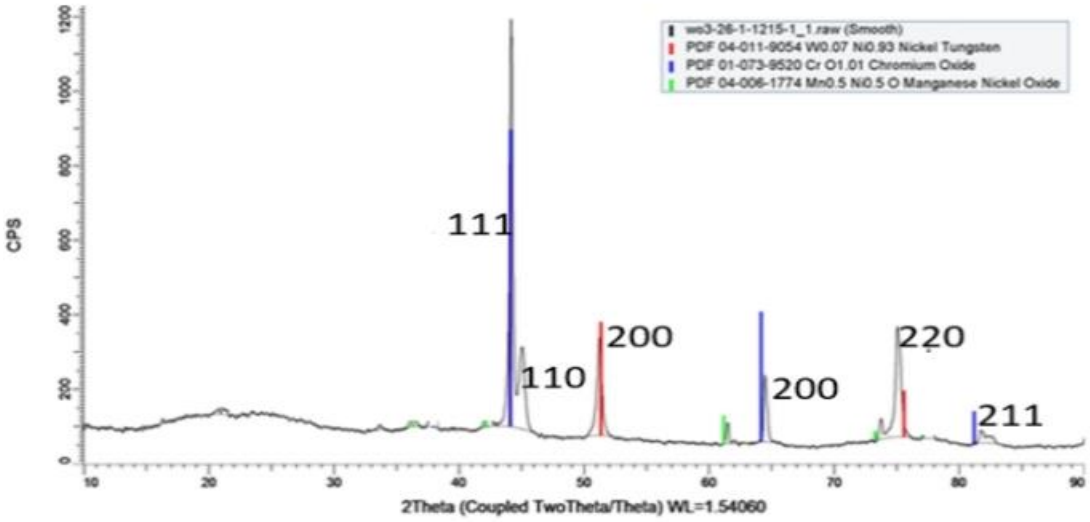

Figure 33. XRD pattern for WO_3 film sample on stainless steel 304 substrate annealed at 300 ℃ for 1 h.

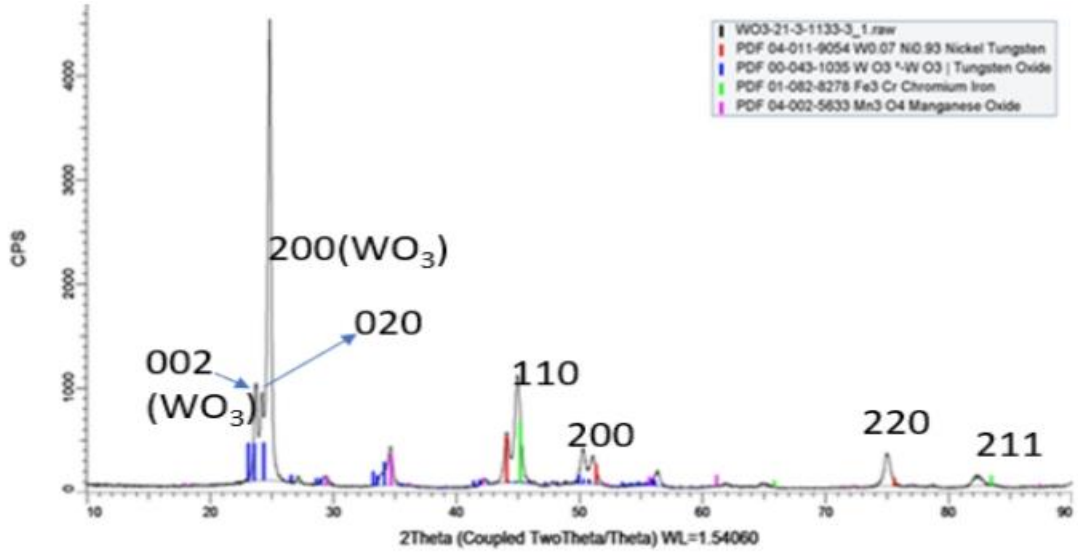

Figure 34. XRD pattern for WO_3 film sample on stainless steel 304 substrate annealed at 400 ℃ for 1 h.

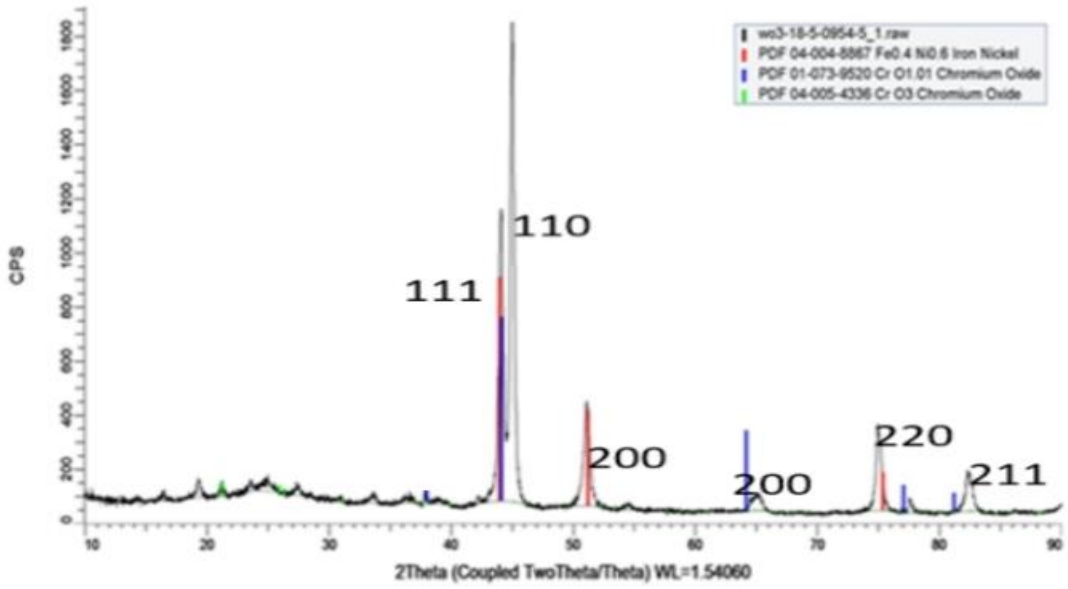

Figure 35. XRD pattern for WO_3 film sample on SS 304 substrate annealed at 500 ℃ for 1 h.

4.10.3 (c) SEM characterization of deposited WO_3 thin film at different annealing temperatures

SEM analysis was done on various samples at a magnification of 500X the as-deposited WO_3 sample (Figure 36a); WO_3 thin film annealed at 200 ℃ (Figure 36b); 300 ℃ (Figure 36c); 400 ℃ (Figure 36d); and 500 ℃ (Figure 36e). From the results obtained, the as-deposited WO_3 sample did not show cracks on the surface as compared to the other samples. The samples annealed at 200 ℃ (Figure 36b) and 300 ℃ (Figure 36c) showed lesser cracks as opposed to samples annealed at 400 ℃ (Figure 36d) and 500 ℃ (Figure 36e), this observation can be due to the amorphous phase of the films at 200 ℃ and 300 ℃ indicating that at these temperatures less loss of water of hydration had occurred. The sample annealed at 400 ℃ shows more cracks on

the surface than samples annealed at 200 ℃ and 300 ℃. These cracks might have been attributed to the strain on the surface that might have occurred during annealing, which led to the phase transition from the amorphous to the monoclinic phase. The water of hydration might have been lost at this temperature, causing more cracks. It is worth noting that the strain might have also occurred due to poor crystallinity and the presence of oxygen vacancies, and this is the likely reason why the film annealed at 500 ℃ had more cracks than at 400 ℃. While the results indicate the presence of cracks, studies by Sharbatdaran et al.[63] suggest that these cracks might not have much effect on the film performance and can be improved through the addition of organic additives.

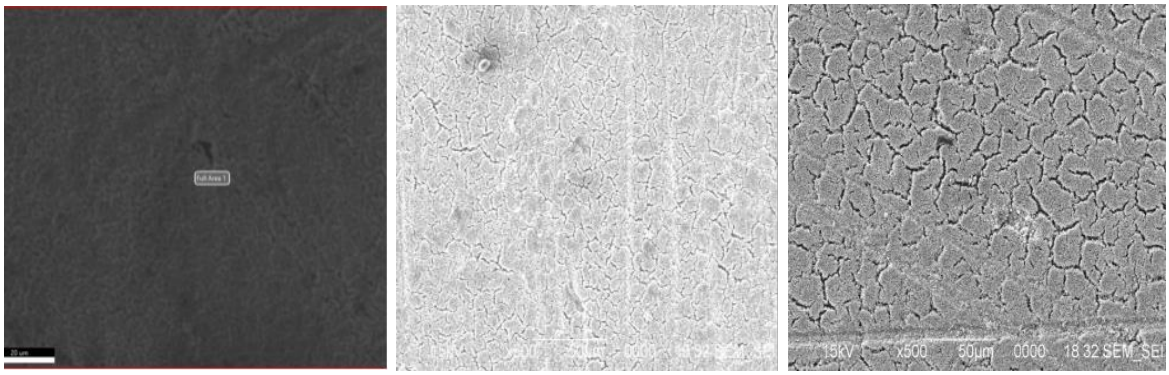

(a) (b) (c)

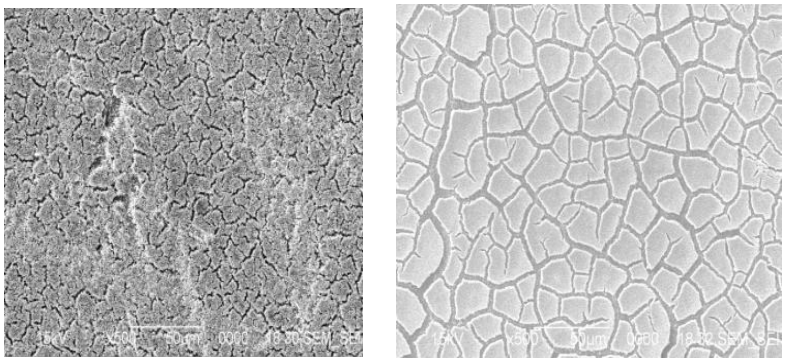

(d) (e)

Figure 36. (a) SEM micrograph of the as-deposited sample, WO_3 film samples annealed at (b) 200 ℃, (c) 300 ℃, (d) 400 ℃, (e) 500 ℃ for 1h respectively at a magnification of X500.

4.11 Photoelectrochemical measurements

The effect of annealing temperature was investigated, whereby the photocurrent densities of the samples were recorded. From the results obtained, it is established that samples annealed at low temperatures tend to record low photocurrent trends. This can be attributed to the lack of crystallinity of nanostructured WO_3 thin films at low temperatures. The cyclic voltammogram in Figure 37 compares different samples annealed at different temperatures. Due to the formation of

different photoactive WO_3 phases at different annealing temperatures, the stability of the nanostructured thin films is attained. Studies indicate that photocurrent density and strength of nanostructured WO_3 influence the photoactivity of WO_3 film.[64] The heat treatment increases the crystal size of WO_3, suppresses electron-hole pair recombination, and causes void reduction. From the results, the sample that was annealed at 400 ℃ recorded the highest photocurrent density.

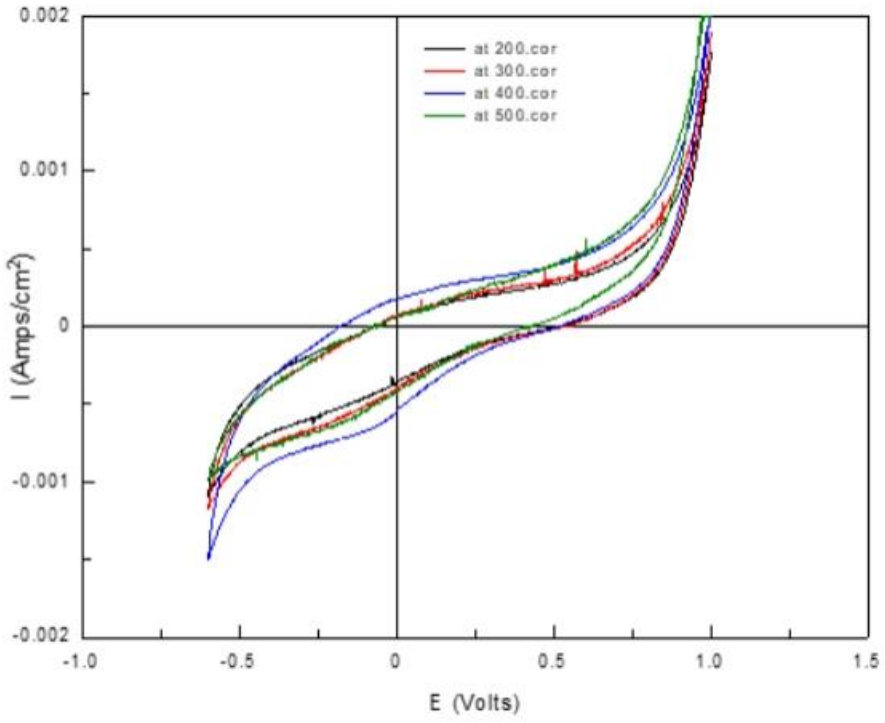

Figure 37. Cyclic voltammograms of WO_3 film on SS 304. Comparing the photocurrent trend at different annealing temperatures at a scan rate of 5 mV/sec, Ag/AgCl, in 0.1 M H_2SO_4.

4.12 Photoactivity measurements

The photoelectrochemical measurements were done under solar illumination at 500 W (Xe lamp (71 mW/cm^2) to determine the photocurrent generation on the WO_3 thin film surfaces. Using 0.530 V as the applied potential, photocurrent densities were obtained by subtracting the dark current from the light current. The voltage at 0.53 V would help to lower the overpotential and this can promote energy efficiency hence cutting down the production cost. As a result, different photocurrent densities were obtained, as shown in Table 5 below.

Table 5. Shows the photocurrent densities obtained from different samples annealed at different temperatures where $V_{applied}$ = 0.530 V vs Ag/AgCl reference.

Sample	Photocurrent at 0.530V in μA/cm^2
Plain stainless steel 304	0.427
WO_3 thin film on SS 304 annealed at 200℃	10.4
WO_3 thin film on SS 304 annealed at 300℃	12.1
WO_3 thin film on SS 304 annealed at 400℃	98.0
WO_3 thin film on SS 304 annealed at 500℃	37.6

The curves in Figures 38-42 show anodic linear sweeps on WO_3 thin film on SS 304 at different annealing temperatures at a scan rate of 5 mV/sec, Ag/AgCl reference electrode, Pt wire counter electrode in 0.1 M H_2SO_4. The results from Table 5. show that plain stainless steel recorded the lowest photocurrent while WO_3 thin films annealed at 200℃ (Figure 39) and 300℃ (Figure 40) showed a weak photocurrent due to the amorphous nature of the film. These amorphous structures are non-photoactive phases. These results agree with the XRD results obtained from

our earlier characterization in which WO_3 film annealed 200 ℃ and 300 ℃ were found to be amorphous. At 400 ℃ (Figure 41), the film showed the highest photocurrent density of about 98 $\mu A/cm^2$, an improvement in photocurrent which is almost ten-fold larger as compared to the films annealed at 200 ℃ and 300 ℃. This improvement in photocurrent density might be attributed to the phase transition from amorphous to monoclinic phase, as earlier reported in XRD characterization in this research. The photocurrent density increase can also be due to a decrease in band gap width in the monoclinic phase so that absorption of more light is enhanced. The narrower band gap can be attributed to a higher concentration of oxygen defects resulting in higher charge generation. At 500 ℃ (Figure 42), a photocurrent of 37.6 $\mu A/cm^2$ was obtained, indicating that at higher temperatures, the film was converted to a hexagonal structure, which is less organized than monoclinic.

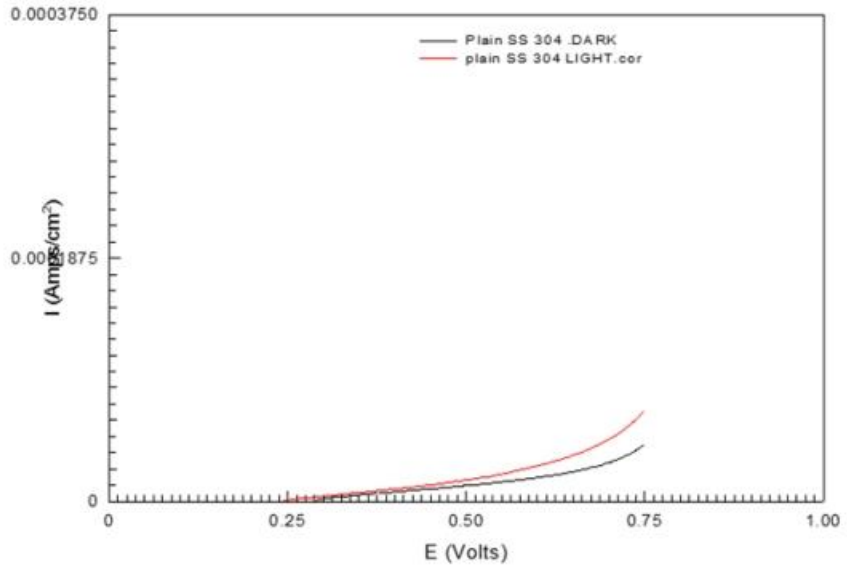

Figure 38. Anodic linear sweep on plain stainless steel at a scan rate of 5 mV/sec, Ag/AgCl, Pt wire, in 0.1 M H_2SO_4.

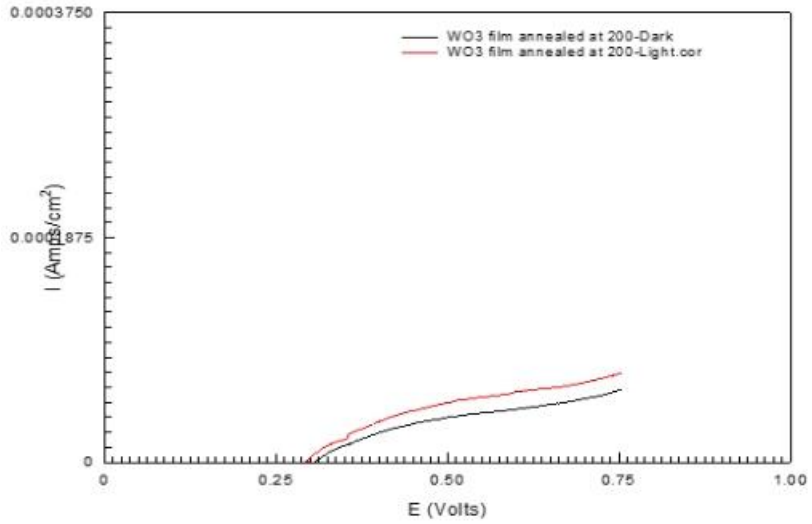

Figure 39. Anodic linear sweeps on WO_3 thin film annealed at 200 ℃ at a scan rate of 5 mV/sec, Ag/AgCl, Pt wire, in 0.1 M H_2SO_4.

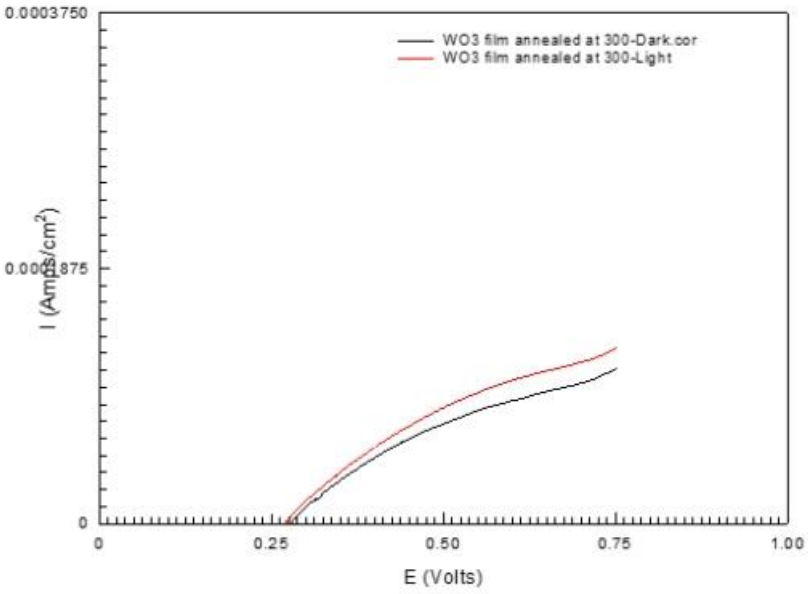

Figure 40. Anodic linear sweeps on WO_3 thin film annealed at 300 ℃ at a scan rate of 5 mV/sec, Ag/AgCl, Pt wire, in 0.1 M H_2SO_4

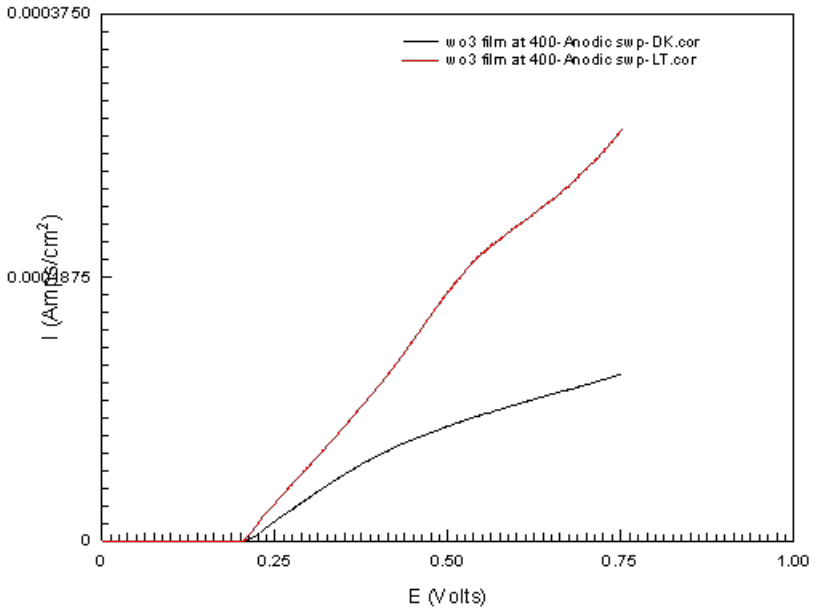

Figure 41. Anodic linear sweeps on WO_3 thin film annealed at 400 °C at a scan rate of 5 mV/sec, Ag/AgCl, Pt wire, in 0.1 M H_2SO_4

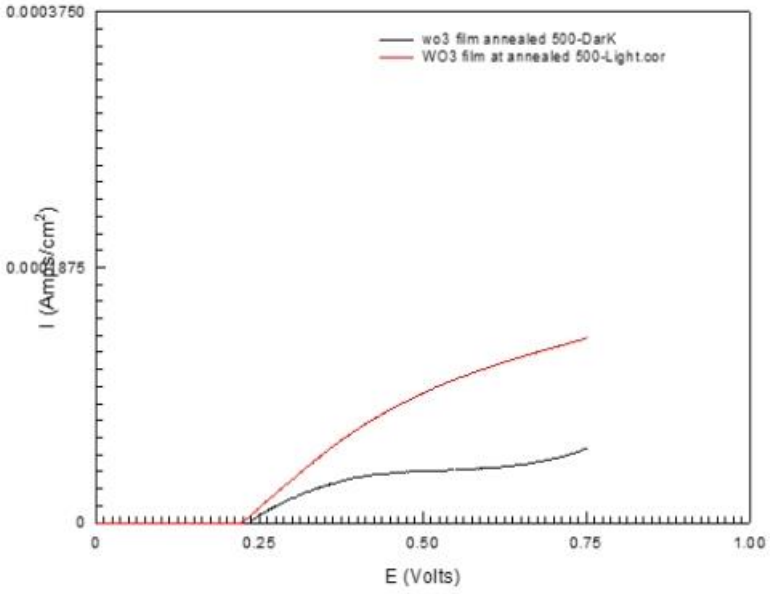

Figure 42. Anodic linear sweeps on WO_3 thin film annealed at 500 °C at a scan rate of 5 mV/sec, Ag/AgCl, Pt wire, in 0.1 M H_2SO_4

4.13 Effect of HNO_3 treatment on WO_3 thin film

To investigate the effect of HNO_3 on the deposited WO_3 thin film, SEM analysis was done. The samples were annealed at different temperatures (200 ℃, 300 ℃, 400 ℃, 500 ℃) In all the analyses done, it was revealed that the thin film whose substrate was not treated in HNO_3 showed more cracks as compared to the one treated in HNO_3 as shown in Figure 43. These samples were annealed at the optimal temperature of 400 ℃.

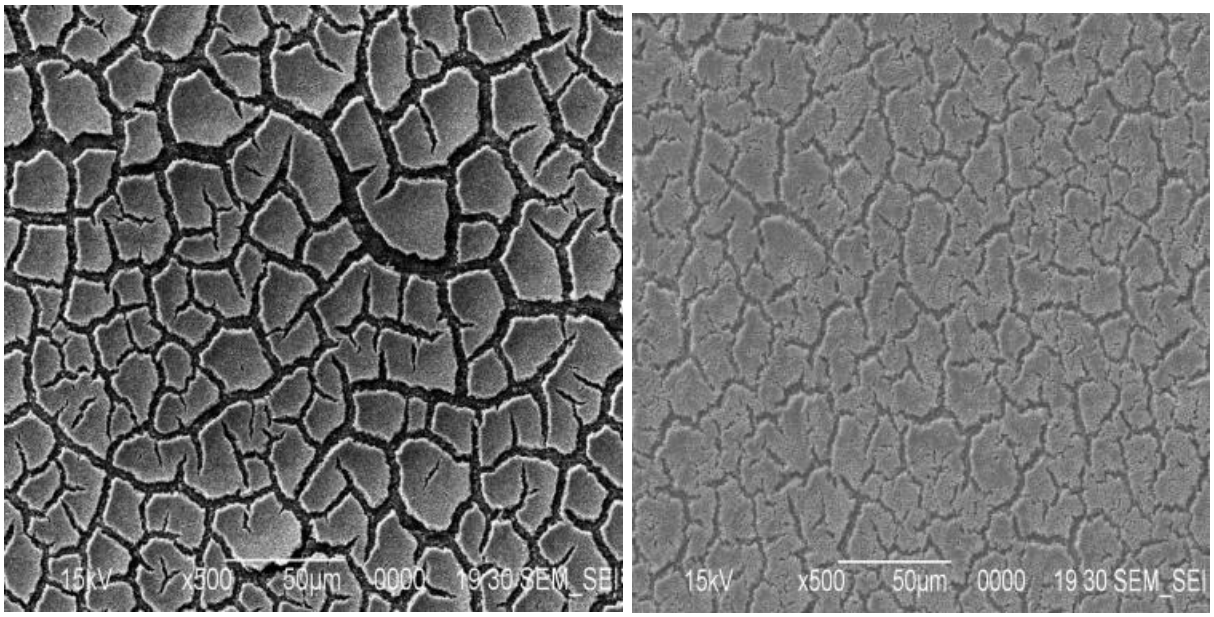

(a) (b)

Figure 43. SEM photos of WO_3 thin films annealed at 400 ℃; (a)substrate not treated in 0.1 M HNO_3 (b) substrate treated in 0.1 M HNO_3.

The photoactivity of these films revealed that the sample not treated with HNO_3 was three times less photoactive than the sample that was treated with HNO_3. Figure 43 shows a comparison of thin films sample whose substrate was not treated in HNO_3. The photocurrent density of

35.5 μA/cm^2 was recorded compared to the one treated with 0.1 M HNO_3 which recorded 98.0μA/cm^2. This might have been caused since HNO_3 passivated the surface of SS 304 by creating a Cr_2O_3 coating.

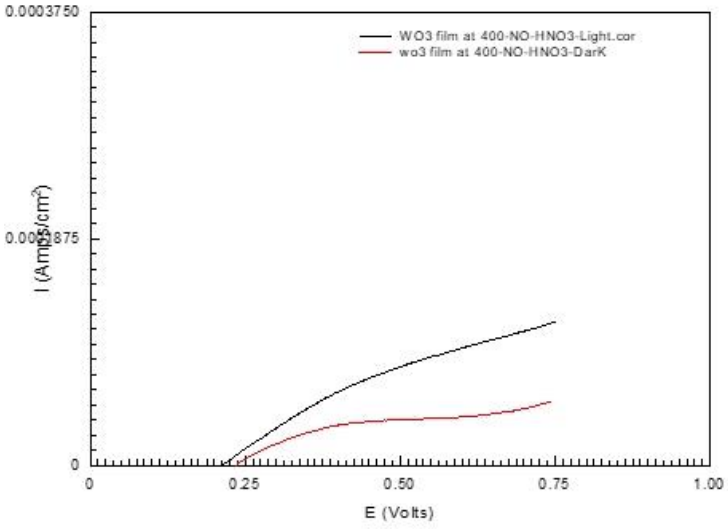

Figure 44. An anodic linear sweep of WO_3 thin film, substrate not treated in HNO_3 annealed at 400℃ at a scan rate of 5 mV/sec, Ag/AgCl, Pt wire, in 0.1 M H_2SO_4.

4.14 WO_3 film on ITO substrate

To compare the behavior of WO_3 thin film on another substrate, WO_3 thin film was deposited on ITO substrate under similar procedures used for SS 304. The result revealed that under similar conditions and at an annealing temperature of 400℃, SS 304 gave slightly better photocurrent density than ITO, which provided a photo density of 78.2 μA/cm^2. When compared with results obtained from the previous research done by Jebet,[43] in which the electrodeposition method was used, WO_3 on ITO gave a photocurrent of 14.4 μA/cm^2 at an applied voltage of 0.658 V. From

this comparison, at lowered applied potential, there was an increased photocurrent energy that can help in enhancing the water-splitting process.

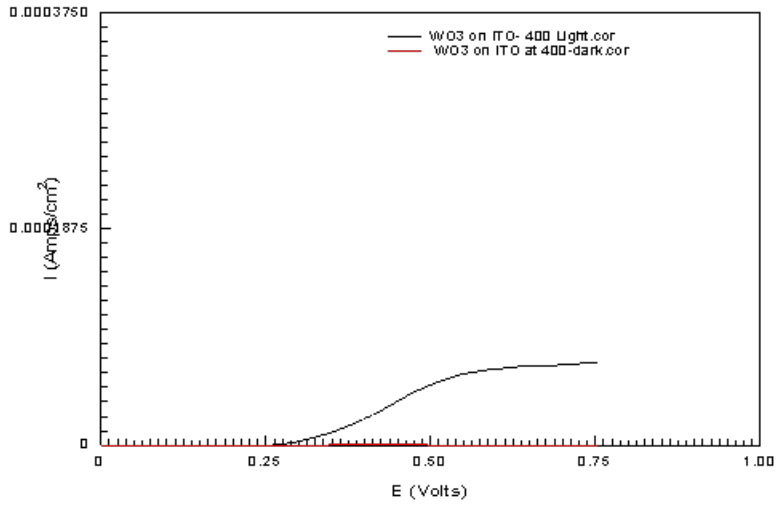

Figure 45. Anodic linear sweeps of WO_3 thin film on ITO substrate annealed at 400 ℃ at a scan rate of 5 mV/sec, Ag/AgCl, Pt wire, in 0.1 M H_2SO_4.

CHAPTER 5. CONCLUSION AND FUTURE WORK

5.1 Conclusion

WO_3 nanostructures have been successfully synthesized using sol-gel, and the effect of annealing temperature was investigated via XRD, SEM, CV, and LSV. The results revealed that the phase and morphology of samples changed with temperature. This study demonstrated that the annealing temperature influences the photoelectrochemical properties of WO_3 thin films. The photoelectrochemical activities correspondingly changed on varying the annealing temperature between 200 ℃ and 500 ℃. XRD results revealed that WO_3 thin films annealed at 200 ℃ and 300 ℃ exhibited an amorphous structure. This amorphous structure gradually crystallized with the increase in annealing temperature to form a monoclinic structure, which was evident at 400 ℃. SEM results indicated that the increase in annealing temperature also resulted in more film cracking. The highest photocurrent density of 98 $\mu A/cm^2$ at an applied voltage of 0.530 V vs Ag/AgCl was attained by the WO_3 thin films annealed at 400 ℃. This photocurrent is about ten times greater than the film annealed at 200 ℃, and an indication that films annealed at 400 ℃ had good crystallinity, optimal particle size, and good connectivity between the particles. The result revealed that it is essential to treat the substrate with HNO_3 to passivate the surface of the stainless steel with a Cr_2O_3 layer. It is worth noting that during sol-gel fabrication, proper sealing of the electrode should be done to enable the sol to spread evenly across the intended surface only. For this reason, doctor blading may not be the best method. However, sol-gel as a fabrication process can be a suitable method to strike a balance between high performance and low fabrication cost in PEC films.

5.2 Future work

A solid foundation has been laid down in understanding the photo enhancement of the deposited film, the effect of cleaning substrate has been studied, and the optimum temperature for annealing the films established. The next generation should consider using a different depositing method, investigate the effects of the aging period of the precursor solution, and try to establish a way of minimizing cracks on the prepared films.

REFERENCES

1. https://www.eia.gov/energyexplained/us-energy-facts/#:~:text=

2. https://www.statista.com/chart/20524/renewable-energy-growth-in-america/

3. Wallner T.“Correlation between Speciated Hydrocarbon Emissions and Flame Ionization Detector Response for Gasoline/Alcohol Blends". J. Eng. Gas Turbines Power, 133(8),2011.

4. Munoz M. Electrochemical Method for Fabrication of Photovoltaic Fibers based on Tungsten Oxide. Master’s thesis Youngstown State University.**2019**.

5. Liao, C. Et al. Hydrogen Production from Semiconductor-based Photocatalysis via Water Splitting.Catalysts.**2012**,2, p 490-516.

6. Bak, T. Et al." Photo-Electrochemical Hydrogen Generation from Water Using Solar Energy. Materials-Related Aspects", Int. J. Hydrogen Energy, **2002**, 27, p 991−1022.

7. Moniz, S. Et al. Visible-light driven heterojunction photocatalysts for water splitting. Energy Environ. Sci. **2015**, 8, p731–759.

8. https://www.quora.com/What-is-the-difference-between-a-valence-band-and-a-conduction-band.

9. Liu, X. Et al. Nanostructure-based WO_3 photoanodes for photoelectrochemical water splitting. Phys. Chem. Chem. Phys. **2012**, 14, p 7894.

10. Krol, R. Et al. Photoelectrochemical Hydrogen Production. Electronic Materials: Science & Technology .**2012**,102, p13-66.

11. Walter, M. Et al. Solar water splitting cells. Chem. Rev. **2010**,110, p 6446–6473.

12. Jiang, C. Et al. Photoelectrochemical devices for solar water splitting – materials and challenges. **2017,** 63, p 4645–4660

13. Bott W, "Electrochemistry of Semiconductors," Curr. Sep**.1998**,17, p 87-92

14. Zhang, Z. Et al. Plasmonic gold nanocrystals coupled with photonic crystal seamlessly on TiO_2 nanotube photoelectrodes for efficient visible light photoelectrochemical water splitting, Nano Lett. **2013**,13, p14–20.

15. Wei, Y. Et al. Polydopamine-assisted decoration of ZnO nanorods with Ag nanoparticles: an improved photoelectrochemical anode, J. Mater. Chem. A, **2013**,87, p5045–5052.

16. Su, F. Et al. Branched TiO_2 nanoarrays sensitized with CdS quantum dots for highly efficient photoelectrochemical water splitting, Phys.Chem. Chem. Phys. **2013,**15, p12026–12032.

17. Gan, J. Et al. Oxygen vacancies promoting the photoelectrochemical performance of In_2O_3 nanocubes, Sci. Rep.**2013**,3, p1021.

18. Kalanur, S. Et al. Facile growth of aligned WO_3 nanorods on FTO substrate for enhanced photoanodic water oxidation activity, J. Mater. Chem. A.**2013**, 18, p3479–3488.

19. Wang, G. Et al. Hydrogen-treated WO_3 nanoflakes show enhanced photostability, Energy Environ. Sci. **2012**, 5, p6180–6187.

20. Wei, W. Et al. Rapid anodic formation of high aspect ratio WO_3 layers with self-ordered nanochannel geometry and use in photocatalysis, Chem. Eur. J. **2012** ,18, p14622–14626.

21. Roselló-Márqueza, G. Et al. Influence of annealing conditions on the photo electrocatalytic performance of WO_3 nanostructures. Separation and Purification Technology. **2020**,238, p11641.

22. Mohamedkhair, A. Et al. Tuning Structural Properties of WO_3 Thin Films for Photo Electrocatalytic Water Oxidation.Catalysts.**2021**, 11, p381.

23. Jurga, J.Et al. Activity of sol-gel derived nanocrystalline WO_3 films in the photoelectrochemical generation of reactive chlorine species. Journal of Electroanalytical Chemistry.**2020,** 871, p11427.

24. Chuanxin, G.Et al. Electron transport and electrochromic properties of sol-gel WO_3 thin films: Effect of crystallinity. Thin Solid Films. **2018**, 119, p 653.

25. Tao, Z. Et al. Electrochemically synthesized tungsten trioxide nanostructures for photoelectrochemical water splitting: Influence of heat treatment on physicochemical properties, photocurrent densities, and electron shuttling. Colloids and Surfaces. **2015,** 484, p 297-303.

26. Samantha, H.Et al. Mesoporous thin film WO_3 photoanode for photoelectrochemical water splitting: a sol-gel dip coating approach. Sustainable Energy Fuels 2017, 1, 145.

27. Mohamed, M.Et al. Synthesis of hexagonal WO_3 nanocrystals with various morphologies and their enhanced electrocatalytic activities toward hydrogen evolution. Direct Science 2018.12.218.

28. Paula, D. Et al. Photoelectrochemical water splitting using WO_3 photoanodes: the substrate and temperature roles.Phys.Chem. **2016**,18, p 5232.

29. Jung, K. Et al. Synthesis of transparent mesoporous tungsten trioxide films with the enhanced photoelectrochemical response: application to unassisted solar water splitting. Energy Environ. Sci., **2011**, 4, p1465.

30. Bin, Y. Et al. Tungsten Trioxide Films with Controlled Morphology and Strong Photocatalytic Activity via a Simple Sol-Gel Route. Catal Lett **.2007** ,118, p 280–284.

31. Yang, J. Et al. Hydrothermal synthesis and photoelectrochemical properties of vertically aligned tungsten trioxide (hydrate) plate-like arrays fabricated directly on FTO substrates, J. Mater. Chem. **2012**, 22, p 17744–17752.

32. Kim, H. Et al.Photoelectrochemical and photocatalytic properties of tungsten oxide nanorods grown by thermal evaporation, Mater. Chem. Phys.**2010,**120, p 452–455.

33. Li, W. Et al. Platelike WO_3 from hydrothermal RF sputtered tungsten thin films for photoelectrochemical water oxidation, Mater. Lett. **2012**,84, p 41–43.

34. Taehwan K. Photoelectrochemical Behavior of WO_3 Electrodeposited on Stainless Steel Microfiber for Flexible, Wire-Shaped Photovoltaic Cells.Youngstown state University.**2022**.

35. Cantalini, C. Et al. Surface electronic properties of polycrystalline WO_3 thin films: a study by core level and valence band photoemission. Surface Science. **2003**, 3(2), p171

36. Deepa, M. Et al. Effect of oxalic acid dihydrate on optical and electrochemical properties of sol–gel derived amorphous electrochromic WO_3 films. **2005,**50, p 3545

37. Habazaki, H. Et al. Characterization of electrodeposited WO_3 films and its application to electrochemical wastewater treatment. Electrochim Acta .**2002**,47, p 4181.

38. Miller, E. Et al. Low-Temperature Reactively Sputtered Tungsten Oxide Films for Solar-Powered Water Splitting Applications.Electrochem SolidState Lett.**2006,** 9(7), p 248

39. Berger, S. Et al. High photocurrent conversion efficiency in self-organized porous WO_3. Appl PhysLett, **2006,** 88, p 311-328.

40. Yamanaka, K.Et al. Peroxotungstic acid-coated films for electrochromic display devices. Japanese Journal of Applied Physics .**1986**,5,p1420–1426.

41. Shen, A. Et al. "A Study of Tungsten Trioxide and Polyaniline Composite Films: I. Electrochemical and Electrochromic Behavior," J. Electrochem. Soc., **1992**. 139, p1840

42. Yang, B. Et al. Enhanced photoelectrochemical activity of sol-gel Tungsten Trioxide films through textural control. Chem.mater. **2007**,19, p 5664-5672.

43. Jebet A. Fabrication of Photovoltaic Thread Using N-Type Tungsten Oxide. Youngstown State University.**2020**.

44. Yang, B.Et al "Novel low-density mesoporous WO_3 films prepared by electrodeposition," Curr. Appl. Phys., **2006**,6(3), p 436-439.

45. Zheng, H. Et al. "Nanostructured tungsten oxide - Properties, synthesis, and applications," Adv. Funct. Mater., **2011**,21(12), p 2175-2196.

46. Feng, J. Et al. Sol-gel synthesis of highly reproducible WO_3 photoanodes for water oxidation. Science China Materials. **2020**, 63(11), p 2261-2271.

47. Teoh, G. Et al. Synthesis of Tungsten Oxide Particles by chemical deposition Method. Material Transactions. **2007**,48(6).1575-1577.

48. Marques, A. Et al. Office Paper Platform for Bioelectrochromic Detection of Electrochemically Active Bacteria using Tungsten Trioxide Nanoprobes: Sci Rep. **2015**,5, p 9910.

49. http://electro-polish.com/processes/passivation/ and https://www.theworldmaterial.com/stainless-steel-chemical-composition/.

50. Chiriac, A. Et al. Sol-Gel Method Performed for Biomedical Products Implementation. Mini reviews in medicinal chemistry. Catalysts. **2018**, 8, p 212.

51. Mackenzie, J. Applications of the Sol-Gel Process.J. Non-Cryst. Solids.**1998**, 100, p162.

52. Madleen, A. Electrochemical properties of Sol-gel WO_3 film Co-doped with Ti and Zi. **2016.**

53. Zhang,S. Nanostructure and thin films and coatings: Functional properties Press, Boca Rotan.**2010**,13,p218.

54. Howatt, L.Et al. Doctor-blade deposition of quantum dots onto standard window glass for low-loss large-area luminescent solar concentrators. Nat. Energy.**2016**, 1, p16157.

55. Mariani, P. Et al. The role of printing techniques for large-area dye-sensitized solar cells. IOP Science Semiconductor and Technology. **2015**,30. p 422.

56. Giannouli, M and G. Leftheriotis, "The effect of precursor aging on the morphology and electrochromic performance of electrodeposited tungsten oxide films." Solar Energy Materials and Solar Cells .**2011**,17, p1932-1939.

57. Zhu, T. Et al. "Nanostructured tungsten trioxide thin films synthesized for photo electrocatalytic water oxidation: a review," Chemsuschem .**2014**,7, p 2974-2997.

58."X-Ray Powder Diffraction (XRD) Techniques".17 Nov. **2022**, serc.carleton.edu/research_education/geochemsheets/techniques/XRD.html.

59. Bish, D and Post, J. Modern Powder Diffraction. Reviews in Mineralogy. Mineralogical Society of America.**1989**,20. p199

60. Scanning Electron Microscope.www.purdue.edu/ehps/rem/images.

61. What is a Surface Profilometer and Surface Profiler Working Principle.www.taylor-hobson.com/resource-center/blog/2018/july/what-is-a-surface-profiler.

62. Peng, W.Et al. Preparation of high-performance ultrafine-grained AISI 304L stainless steel under high temperature.**2016**,26, p 404-410.

63. Sharbatdaran, M.Et al. Preparation and characterization of WO_3. Chem. Eng.**2006**,2, p 25.

64. Gustavo, C. et al.Oxidation Behavior of stainless steel 304 and 316 under atmospheric surface conditions. Corrosion Science.**2018**,5, p132.

65. Memar, A. Et al. Optimization and characterization of biomolecule immobilization on silicon substrates. Applied surface science.**2014**, 305,p 522-530.

66. C.Guillen and J. Herreror.Amorphous WO_{3-x} thin films with color characteristics tuned by the oxygen vacancies created during reactive DC sputtering.Journal of Materials Science & Technology.**2021**,78,p 223-228